

**ECOLE POLYTECHNIQUE**

**CENTRE DE MATHÉMATIQUES APPLIQUÉES**

*UMR CNRS 7641*

---

91128 PALAISEAU CEDEX (FRANCE). Tél: 01 69 33 46 00. Fax: 01 69 33 46 46  
<http://www.cmap.polytechnique.fr/>

**NUMERICAL SIMULATION OF OF  
TRANSCRITICAL STRAINED  
LAMINAR FLAMES**

Vincent Giovangigli and Lionel Matuszewsky

**R.I. 730**

*Novembre 2011*

# Numerical simulation of transcritical strained laminar flames

Vincent Giovangigli<sup>1,2</sup> and Lionel Matuszewski<sup>2\*</sup>

<sup>1</sup>CMAP-CNRS, Ecole polytechnique, Palaiseau, France

<sup>2</sup>ONERA DEFA, 6 chemin de la Hunière, Palaiseau, France

## Abstract

We investigate reactive and non reactive strained flows associated with high pressure cryogenic rocket engines. A detailed high pressure fluid model based on thermodynamics of irreversible processes, statistical mechanics as well as kinetic theory of dense gases is used. This model insures the positivity of chemical entropy production and of molecular transport related entropy production. We first study the structure of a pseudo-vaporizing transcritical oxygen layer and the corresponding pseudo-vaporizing rates. We next investigate a mixing layer between cold hydrogen and oxygen and the dramatic influence of nonideal transport near thermodynamic instabilities. Diffusion and partially premixed H<sub>2</sub>-O<sub>2</sub> transcritical flame structures are then studied as well as strain extinction limits and dilution extinction limits.

## 1 Introduction

High pressure combustion has been used for quite a long time in order to increase the thermodynamical efficiency of automotive and rocket engines. This motivates the study of strained laminar flames [1, 2, 3, 4] associated with turbulent combustion models [5, 6, 7] in the context of nonideal reactive mixture. Following the work of Saur *et al.* [8], El-Gamal *et al.* [9], Ribert *et al.* [10] and Pons *et al.* [11, 12], the purpose of this paper is to further study the influence of pressure driven nonidealities on H<sub>2</sub>-O<sub>2</sub> mixing layers and H<sub>2</sub>-O<sub>2</sub> flame structures.

The high pressure flame model combines a real gas thermodynamics based on the Soave-Redlich-Kwong equation of state [13], nonideal chemical production rates and nonideal transport fluxes [14]. The Soave-Redlich-Kwong equation of state is widely used for the modeling of transcritical flows, in particular by Ribert *et al.* [10] and Zong and Yang [15, 16] and yields a good representation of dense to dilute fluids. For radical species, the evaluation of attractive and repulsive terms of the equation of state uses molecular considerations similar to the one used by Saur *et al.* [8] and El-Gamal *et al.* [9].

Molecular transport fluxes for dense fluid are based on the thermodynamics of irreversible processes [17, 18, 19, 20], statistical mechanics [21, 22, 23], statistical thermodynamics [24] and on kinetic theory of dense gases [25, 26, 27]. These flux insure the positivity of the transport related entropy production independently of the thermodynamic model. Nonideality in diffusion driving forces have already been used by Okong'o and Bellan [28], Oefelein [29], Bellan [30] and the authors [14] with coefficients taking into account steric effects arising at high densities.

The nonideal chemical production rates that are used have first been introduced by Marcelin [31, 32] and rederived from nonequilibrium statistical thermodynamics by Keizer [24]. They are compatible with the symmetric forms of rates of progress obtained through kinetic theory for dilute gases [33, 34] and insure the positivity of chemical entropy production. This formulation has been compared to other widely used formulations for planar flames [14] and its influence has been found to range from a few percent at pressures around 100 atm to 25% percent at pressure of 1000 atm.

The whole high pressure flame model is used to perform simulation of laminar strained reactive as well as non-reactive structures of interest for cryogenic turbulent combustion.

First we study the influence of the transport coefficients on the pseudo-vaporization mass rate per unit surface of transcritical oxygen. We show that, despite the fact that this influence is not negligible, the pseudo-vaporization mass rate stays closely related to the pseudo-Spalding parameter introduced by Yang [35] for varied expressions of the molecular transport coefficients.

We then study a strained mixing layer between cold H<sub>2</sub> and cold O<sub>2</sub> at supercritical pressure. We show that the inclusion of nonidealities in the diffusion driving force is able to reproduce the

---

\*Corresponding author. E-mail: lionel.matuszewski@onera.fr

lack of miscibility between these two species near chemical thermodynamical instability. Neglecting these nonidealities results in an erroneous structure in which some unstable — and thus unphysical — thermodynamical states appear in the computational domain. The nearly non-miscibility of  $\text{H}_2$  and  $\text{O}_2$  for high pressure and low temperature results in stiff concentration and density gradients inside the mixing layer and the appearance of a quasi interface in contrast with the mild gradients of the erroneous ideal transport solution.

Diffusion strained flame between dense cold liquid-like oxygen and gas-like fuel are then investigated. This kind of flame structure is likely to appear in a rocket engine running at supercritical pressure in the wake of the injection device, where dense oxygen cluster are striped from the main core and undergo rapid heating and burning. The fuel side of the flame is either pure hydrogen at the injection condition in the immediate wake of the injector and hydrogenated combustion products downstream in the combustion chamber. These combustion phenomenon are emblematic of high fuel ratio running engines and their behaviours are of great interest in the understanding of the whole combustion process. We study here two characteristic flame structures — respectively an  $\text{H}_2\text{-O}_2$  diffusion flame and a  $(\text{H}_2+\text{H}_2\text{O})\text{-O}_2$  diffusion flame — in a nonideal framework.

In the presence of local extinction phenomena or in the early stage of engine ignition, oxygen and fuel are not necessary separated by a flame sheet and premixed combustion is likely to occur. Stability of the premixed flame structures influences the stability of the whole combustion process as these structures are part of the forefront of reignition phenomena. We study the structure of the flame established between a gas-like fuel-rich  $\text{H}_2\text{-O}_2$  mixture and dense cold  $\text{O}_2$ . These structures are composed of two different combustion zones, respectively a premixed combustion zone and a diffusion combustion zone. Depending on the stretch rate and on the premixed mixture temperature, these zones are more or less far appart and some structures, in which two flames are separated by combustion products, are then computed as emblematic of reignition processes.

We finally study the stability of diffusion flames between liquid-like cold oxygen and gas-like fuel in order to determine in which conditions local extinction phenomena may occur. We first compute the dilution extinction limits of diffusion flames between a mixture of  $\text{H}_2$  in combustion products — modeled by  $\text{H}_2\text{O}$  — and  $\text{O}_2$  by varying the dilution rate of hydrogen inside water at a fixed stretch rate. These extinction phenomena occur when turbulent mixing process is not great enough to rip the combustion product layer growing between oxygen and hydrogen. We then compute the stretch extinction limit of these flames by varying the strain rate in order to grasp the ability of turbulence to quench the combustion process. Using continuation procedures, solution curves are obtained and two distinct behaviour were shown. Strain rate dependent solution curves are typically S-shaped with both ignition and extinction point whereas dilution rate dependent solution curves are S-shaped and C-shaped respectively for low and high strain rate. The C-shaped dependency curves indicate that the burning and extinguished solution branches are no longer connected, and hence that spontaneous reignition is difficult in highly turbulent flows. We then determine the flammability domain of cold  $\text{H}_2\text{-O}_2$  mixtures in a turbulent context to measure their reignition capabilities.

In Section 2 we describe the high pressure strained flame model. Strained mixing layer are addressed in Section 3 and 4. Section 5 is devoted to the simulation of transcritical strained diffusion flames whereas Section 6 is focused on the case of transcritical partially premixed stretched flames. Finally extinction limits of transcritical strained diffusion flames are studied in Section 7

## 2 High pressure model

In this section we briefly describe the detailed high pressure flame model used thorough this study. This model is similar to the one previously used for planar premixed flame computations [14] and is based on thermodynamics of irreversible processes [17, 18, 19, 20], on statistical thermodynamics [24] and on molecular theories such as statistical mechanics [21, 22, 23] and kinetic theory of dense gases [25, 26, 27].

## 2.1 Conservation equations

The steady conservation equations governing stretched laminar flames under the small Mach number approximation are in the form

$$\rho\varepsilon\tilde{u} + (\rho v)' = 0, \quad (1)$$

$$\rho v\tilde{u}' + \varepsilon(\rho\tilde{u}^2 - \rho^{\text{up}}) - (\eta\tilde{u}')' = 0, \quad (2)$$

$$\rho v Y_i' + \mathcal{F}_i' = m_i \omega_i, \quad i \in \mathcal{S}, \quad (3)$$

$$\rho v h' + q' = 0, \quad (4)$$

where  $v$  is the velocity of the fluid in the direction normal to the flame surface,  $\rho$  is the mixture density and  $\varepsilon$  is the strain rate. The tangential velocity  $u$  is written in the form  $u = \varepsilon y \tilde{u}$  where  $y$  denotes the tangential coordinate, the superscript  $'$  denotes the derivative with respect to the normal coordinate  $x$  and the superscript  $^{\text{up}}$  correspond to value taken at the boundary  $x = +\infty$ . The symbol  $Y_i$  represents the mass fraction of species  $i$ ,  $\mathcal{F}_i$  the diffusion flux of species  $i$  in the direction normal to the flame,  $m_i$  the molar mass of species  $i$ ,  $\omega_i$  the molar chemical production for species  $i$ ,  $\mathcal{S} = \{1, \dots, n^s\}$  the species indexing set with  $n^s$  the number of species,  $\eta$  and  $h$  respectively the shear viscosity and the enthalpy per unit mass of the mixture and  $q$  the heatflux.

The boundary conditions at the far-field boundaries read

$$\begin{aligned} T(+\infty) &= T^{\text{up}}, \\ Y_i(+\infty) &= Y_i^{\text{up}}, \quad i \in \mathcal{S} \\ \tilde{u}(+\infty) &= 1 \\ T(-\infty) &= T^{\text{do}}, \\ Y_i(-\infty) &= Y_i^{\text{do}}, \quad i \in \mathcal{S} \\ \tilde{u}(-\infty) &= \sqrt{\rho^{\text{up}}/\rho^{\text{do}}}, \end{aligned}$$

where  $T$  is the temperature of the mixture and the superscripts  $^{\text{do}}$  and  $^{\text{up}}$  indicate values taken at the boundary  $x = -\infty$  and  $x = +\infty$  respectively. Finally, the normal velocity vanishes at the stagnation point located at the origin

$$v(0) = 0.$$

Under the assumption of low Mach number, the normal momentum equation uncouples from the other equation and may only be useful to evaluate a vertical pressure perturbation [34].

## 2.2 Thermodynamics properties

Dense fluids thermodynamics is obtained from a given pressure law by assuming that Gibbs' relationships are satisfied and that the fluid has a perfect gas behaviour at the dilute gas limit. This procedure is classical [36, 37, 38] and yields a unique thermodynamics on the whole range of density predicted by the pressure law [39]. Many equations of state have been proposed to grasp the complex behaviour of dense fluids [8, 13, 40, 41, 42, 43, 44]. The Benedict-Webb-Rubin equation of state [40, 41] displays great accuracy whereas its evaluation is quite computationally expensive. Thanks to an easier inversion through Cardan's formula, the cubic equations of state as the Soave-Redlich-Kwong [42, 13] and the Peng-Robinson [43, 44] equations are often used and yield accurate results over the range of pressures, temperatures and mixtures states encountered in supercritical running rocket engine [29].

We use here the Soave-Redlich-Kwong equation of state [42, 13], hereafter labelled SRK, which reads

$$p = \sum_{i \in \mathcal{S}} \frac{Y_i}{m_i} \frac{RT}{v - b} - \frac{a}{v(v + b)},$$

where  $p$  is the fluid pressure,  $R$  the perfect gas constant,  $v = 1/\rho$  the volume per unit mass and  $a$  and  $b$  the attractive and repulsive parameters per unit mass respectively. The attractive parameter depends on the temperature and the fluid composition whereas the repulsive parameter depends solely on the composition. They are evaluated with the Van der Waals mixing rules

$$\begin{aligned} a(Y_1, \dots, Y_{n^s}, T) &= \sum_{i, j \in \mathcal{S}} Y_i Y_j \sqrt{a_i a_j}, \\ b(Y_1, \dots, Y_{n^s}) &= \sum_{i \in \mathcal{S}} Y_i b_i, \end{aligned}$$

where the pure-species parameters  $a_i(T)$  and  $b_i$ ,  $i \in \mathcal{S}$  evaluation is based on critical data considerations. For a chemically stable compound, these pure-species parameters may be evaluated in the form [13, 38]

$$a_i(T_{c,i}) = 0.42748 \frac{R^2 T_{c,i}^2}{m_i p_{c,i}}, \quad b_i = 0.08664 \frac{R T_{c,i}}{m_i p_{c,i}},$$

where  $T_{c,i}$  and  $p_{c,i}$  denote the critical temperature and pressure respectively of species  $i$ . As pointed out in [14], such a procedure is irrelevant in the case of chemically unstable species for which pure-species states cannot be obtained down to critical condition. However, it is possible to relate macroscopic behaviour with molecular interaction parameters and thus write attractive and repulsive parameters in terms of these molecular interaction parameters. Assuming a Lennard-Jones shape of the molecular interaction potential, one may estimate the critical volume per unit mass  $v_{c,i}$  and the critical temperature  $T_{c,i}$  [45, 46, 47] and finally obtain the following evaluation

$$a_i(T_{c,i}) = (5.55 \pm 0.12) \frac{N^2 \epsilon_i \sigma_i^3}{m_i^2}, \quad b_i = (0.855 \pm 0.018) \frac{N \sigma_i^3}{m_i},$$

with  $N$  the Avogadro number,  $\epsilon_i$  and  $\sigma_i$  the Lennard-Jones potential well depth and molecular diameter of species  $i$ , respectively. The SRK equation of state could thus solely be based on molecular potential parameters as the equation of state used by Saur [8] and El-Gamal [9]. This feature is closely related with the assumption of interaction potential in the form  $\epsilon \phi(r/\sigma)$  — where  $\epsilon$  and  $\sigma$  are the potential well depth and the collision diameter respectively — which underlies the corresponding states principle [37, 48]. However, as discussed in [14], we choose not to extend the molecular definition of attractive and repulsive parameter to the stable species case for accuracy sake since these species do not strictly follow a Lennard-Jones behaviour.

The temperature dependency of the pure species attractive parameter is expressed through the classical Wilson form [49]

$$a_i(T) = a_i(T_{c,i}) \alpha_i(T_i^*),$$

where  $\alpha_i$  a non-negative function of the reduced temperature  $T_i^* = T/T_{c,i}$  with respect to species  $i$ . The function  $\alpha_i$  is such that  $\alpha_i(1) = 1$  and, following Grabovski and Daubert [50] and Ozokwelu and Erbar [51], is a decreasing function of  $T_i^*$ . As discussed in [14], the original Soave determination [13]  $\sqrt{\alpha_i} = |1 + s_i(1 - \sqrt{T_i^*})|$ ,  $i \in \mathcal{S}$  with  $s_i = 0.48508 + 1.5517\varpi_i - 0.151613\varpi_i^2$  — where  $\varpi_i$  is the acentric factor of species  $i$  — has been slightly modified into  $\sqrt{\alpha_i} = 1 + \mathcal{A}(s_i(1 - \sqrt{T_i^*}))$ . The  $\mathcal{A}$  function insures the decreasing property of  $\alpha_i$  in a smooth way. To obtain the continuity of the first and second derivatives of  $\sqrt{\alpha_i}$ , we have used  $\mathcal{A}(z) = z$  if  $z \geq 0$  and  $\mathcal{A}(z) = z/(1 + z^4)^{1/4}$  if  $z < 0$ . The smoothing procedure does not alter much the fluid behaviour as it is inactive for reduced temperatures lower than unity — that is to say in the domain in which the Soave calibration was made — and since it does not modify appreciably the pure species attractive parameter temperature dependency in the vicinity of the critical temperature  $T_{c,i}$ . For greater temperatures, the influence of the attractive parameter quickly decreases and the smoothing procedure is of no consequence. Nevertheless, this procedure removes inconsistencies in the temperature dependency and avoids spurious behaviour of numerical methods which require smooth thermodynamical functions.

From the pressure law it is then possible to determine the corresponding Gibbsian thermodynamic. As an example, we give here the expression of the fluid enthalpy and entropy, as deduced from SRK equation

$$\begin{aligned} h &= \sum_{i \in \mathcal{S}} Y_i [h_i^{\text{st}} + \int_{T^{\text{st}}}^T c_{p,i}(\theta) d\theta] + \frac{T \partial_T a - a}{b} \ln\left(1 + \frac{b}{v}\right) + \sum_{i \in \mathcal{S}} \frac{Y_i}{m_i} \frac{RTb}{v - b} - \frac{a}{v + b}, \\ s &= \sum_{i \in \mathcal{S}} Y_i [s_i^{\text{st}} + \int_{T^{\text{st}}}^T \frac{c_{p,i}(\theta)}{\theta} d\theta] - \frac{R}{m_i} \ln\left(\frac{Y_i RT}{(v - b)p^{\text{st}}}\right) + \frac{\partial_T a}{b} \ln\left(1 + \frac{b}{v}\right), \end{aligned}$$

where the superscript <sup>st</sup> denotes the standard state.

### 2.3 Molecular transport fluxes

The model for molecular transport fluxes is derived from thermodynamics of irreversible processes [17, 18, 19, 20], statistical mechanics [21, 22, 23] as well as statistical thermodynamics [24] and kinetic

theory of dense gases [25, 26, 27]. The expressions given in this section are expressed in a one-dimensional formalism since, in the scope of laminar stretched flame, the diffusion fluxes only appear in the direction normal to the flame. The mass and heat fluxes are given by the expressions

$$\mathcal{F}_i = - \sum_{j \in \mathcal{S}} L_{ij} \left( \frac{g_j}{T} \right)' - L_{iq} \left( -\frac{1}{T} \right)', \quad i \in \mathcal{S}, \quad (5)$$

$$q = - \sum_{j \in \mathcal{S}} L_{qj} \left( \frac{g_j}{T} \right)' - L_{qq} \left( -\frac{1}{T} \right)', \quad (6)$$

where  $g_i$  is the chemical potential of species  $i$  per unit mass, the superscript  $'$  denotes the derivative with respect to the coordinate  $x$  normal to the flame and  $L_{ij}$ ,  $i, j \in \mathcal{S} \cup \{q\}$  are the transport coefficients. The matrix  $L$  with coefficients  $L_{ij}$ ,  $1 \leq i, j \leq q = n^s + 1$  is symmetric positive semi-definite with null-space  $N(L) = \mathbb{R}\mathcal{U}$  with  $\mathcal{U} = (1, \dots, 1, 0)^t \in \mathbb{R}^{n^s+1}$ . The coefficients  $L_{ij}$  can be written in term of the transport coefficients used in classical transport fluxes formulation. To do so, it is necessary to rewrite the fluxes (5) and (6) with generalized diffusion driving force. To this aim, we introduce  $\mu_j = m_j g_j / RT$ ,  $j \in \mathcal{S}$ , the dimensionless chemical potentials and we have

$$d\mu_j = \frac{m_j v_j}{RT} dp + \sum_{l \in \mathcal{S}} \partial_{X_l} \mu_j dX_l - \frac{m_j h_j}{RT^2} dT,$$

where  $v_j$  is the partial volume per unit mass of species  $j$ ,  $X_l$  the mole fraction of species  $l$ ,  $h_j$  the enthalpy per unit mass of species  $j$ , and  $d$  the total differential operator. We may now introduce the generalized diffusion driving force  $d_j$  as

$$d_j = X_j (\mu_j)'_T = \frac{X_j m_j v_j}{RT} p' + \sum_{l \in \mathcal{S}} \Gamma_{jl} X_l',$$

where  $(\mu_j)'_T$  denotes the gradient of the dimensionless chemical potential taken at constant temperature and  $\Gamma_{jl} = \partial_{X_l} \mu_j$ ,  $l, j \in \mathcal{S}$ . In the isobaric context which will be used hereafter, we can further introduce the ideal and nonideal contributions to the generalized diffusion driving force  $d_j$  by splitting the dimensionless chemical potential  $\mu_i$  into a singular ideal part  $\ln X_i$  and a smooth nonideal part  $\mu_i^{\text{sm}}$ . The generalized diffusion driving force then reads

$$d_i = X_i (\mu_i)'_T = X_i' + X_i (\mu_i^{\text{sm}})'_T,$$

and  $X_i'$  stand for the ideal contribution. The nonideal contribution is proportional to the gradient  $(\mu_i^{\text{sm}})'_T$  taken at constant temperature which allows to simplify the numerical evaluation of the fluxes [14].

In term of these generalized driving forces, the mass and heat fluxes now read

$$\mathcal{F}_i = - \sum_{j \in \mathcal{S}} \frac{\hat{L}_{ij} R}{X_j m_j} d_j - \frac{\hat{L}_{iq}}{T^2} T', \quad i \in \mathcal{S}, \quad (7)$$

$$q - \sum_{i \in \mathcal{S}} h_i \mathcal{F}_i = - \sum_{j \in \mathcal{S}} \frac{\hat{L}_{qj} R}{X_j m_j} d_j - \frac{\hat{L}_{qq}}{T^2} T', \quad (8)$$

where the transport coefficient have been modified from the matrix  $L$  into the matrix  $\hat{L}$  given by  $\hat{L} = A^t L A$  where  $A_{ij} = \delta_{ij}$ ,  $1 \leq i, j \leq q = n^s + 1$ , to the exception of  $\{i, j\} \in \mathcal{S} \times \{q\}$  for which  $A_{iq} = -h_i$ . Expressions (7) and (8) for transport fluxes then allow the identification of the modified transport coefficients  $\hat{L}$  with the generalized diffusion coefficient  $D_{ij}$ ,  $i, j \in \mathcal{S}$  introduced by Kurochkin [27] and extending the symmetric coefficient for dilute gases of Waldmann [52, 53, 54, 55], the thermal diffusion coefficients  $\theta_i$  and the partial thermal conductivity  $\hat{\lambda}$ . This identification leads to the definitions

$$\frac{\hat{L}_{ij} R}{\rho Y_i Y_j \bar{m}} = D_{ij}, \quad i, j \in \mathcal{S}, \quad \frac{\hat{L}_{iq}}{T} = \rho Y_i \theta_i, \quad \frac{\hat{L}_{qq}}{T^2} = \hat{\lambda},$$

where  $\bar{m} = \sum_{l \in \mathcal{S}} X_l m_l / \sum_{l \in \mathcal{S}} X_l$  is the mean molar mass of the mixture. The properties of the matrices  $L$  and  $\hat{L}$  are then transmitted to the transport coefficients in a way that we have the symmetry relations  $D_{ij} = D_{ji}$ ,  $i, j \in \mathcal{S}$ , the mass constraints  $\sum_{j \in \mathcal{S}} D_{ij} Y_j = 0$ ,  $i \in \mathcal{S}$ ,  $\sum_{i \in \mathcal{S}} \theta_i Y_i = 0$ , and the matrix

$D$  is positive semi-definite with null-space  $N(D) = \mathbb{R}\mathbf{y}$ , where the mass fraction vector defined by  $\mathbf{y} = (Y_1, \dots, Y_{n^s})^t$ . Using the above defined coefficients, the fluxes (7) and (8) are rewritten in the classical form

$$\begin{aligned}\mathcal{F}_i &= -\sum_{j \in \mathcal{S}} \rho Y_i D_{ij} d_j - \rho Y_i \theta_i (\ln T)', \quad i \in \mathcal{S}, \\ q &= \sum_{i \in \mathcal{S}} h_i \mathcal{F}_i - \frac{\rho R T}{\bar{m}} \sum_{j \in \mathcal{S}} \theta_j d_j - \hat{\lambda} T'.\end{aligned}$$

It is also possible to express the heat flux in term of the mass fluxes by introducing the generalized thermal diffusion ratios  $\chi_i$ ,  $i \in \mathcal{S}$ , defined by the relations  $\theta_i = \sum_{j \in \mathcal{S}} D_{ij} \chi_j$ , and the constraint  $\sum_{j \in \mathcal{S}} \chi_j = 0$  and defining the thermal conductivity  $\lambda$  by

$$\lambda = \hat{\lambda} - \frac{\rho R}{\bar{m}} \sum_{i, j \in \mathcal{S}} D_{ij} \chi_i \chi_j.$$

Using the thermal diffusion ratios  $\chi_i$  and the thermal conductivity  $\lambda$ , the molecular fluxes are given by

$$\begin{aligned}\mathcal{F}_i &= -\sum_{j \in \mathcal{S}} \rho Y_i D_{ij} (d_j + X_j \tilde{\chi}_j (\ln T)'), \quad i \in \mathcal{S}, \\ q &= \sum_{i \in \mathcal{S}} (h_i + \frac{R T \tilde{\chi}_i}{m_i}) \mathcal{F}_i - \lambda T',\end{aligned}$$

with  $\tilde{\chi}_i = \chi_i / X_i$ .

## 2.4 Chemical production rates

The expression for the rates of progress can be deduced from statistical thermodynamics considerations [24] and, to the author's knowledge, was first introduced by Marcelin [31, 32]. This formulation, in the following called the symmetric formulation, insures the positivity of the chemical entropy source term [14]. Under the perfect gas assumption it reduces to the classical mass action law. We consider a general reaction mechanism described by the relations



where  $\nu_{ij}^f$  and  $\nu_{ij}^b$  are the forward and backward stoichiometric coefficients of species  $i$  involved in reaction  $j$ ,  $\mathcal{M}_i$  is the symbol of species  $i$  and where  $\mathcal{R} = \{1, \dots, n^r\}$  denotes the set of reaction indexes with  $n^r$  the number of reactions. The molar production rate  $\omega_i$  of species  $i$  is then classically evaluated by summing the contributions of each reaction

$$\omega_i = \sum_{j \in \mathcal{R}} (\nu_{ij}^b - \nu_{ij}^f) \tau_j,$$

where  $\tau_j$  denotes the rate of progress of the  $j$ th reaction. The nonideal formulation for the rate of progress reads

$$\tau_j = \kappa_j^s \left( \exp \left( \sum_{i \in \mathcal{S}} \nu_{ij}^f \mu_i \right) - \exp \left( \sum_{i \in \mathcal{S}} \nu_{ij}^b \mu_i \right) \right), \quad (9)$$

where  $\kappa_j^s$  is the reaction constant, hereafter labelled the "symmetric" reaction constant, which generally depends only on temperature and may thus be deduced from the low density limit where thermodynamics is essentially the one of the perfect gas.

In order to show the relationship between the symmetric reaction constant and the classical reaction constants, we investigate here the rate of progress in the framework of perfect gases. Under these assumptions, the dimensionless chemical potential can be written under the form  $\mu_i^{\text{PG}} = \mu_i^{\text{u,PG}} + \ln \gamma_i^{\text{PG}}$ ,  $i \in \mathcal{S}$ , where  $\mu_i^{\text{u,PG}}$  is the perfect gas dimensionless chemical potential of species  $i$  at unity molar concentration. The rate of progress for perfect gases  $\tau_j^{\text{PG}}$  can now be written under the generalized formulation

$$\tau_j^{\text{PG}} = \kappa_j^s \exp \left( \sum_{i \in \mathcal{S}} \nu_{ij}^f \mu_i^{\text{u,PG}} \right) \prod_{i \in \mathcal{S}} (\gamma_i^{\text{PG}})^{\nu_{ij}^f} - \kappa_j^s \exp \left( \sum_{i \in \mathcal{S}} \nu_{ij}^b \mu_i^{\text{u,PG}} \right) \prod_{i \in \mathcal{S}} (\gamma_i^{\text{PG}})^{\nu_{ij}^b},$$

in such a way that we recover the usual forward  $\kappa_j^f$  and  $\kappa_j^b$  backward reaction constants

$$\kappa_j^f = \kappa_j^s \exp\left(\sum_{i \in \mathcal{S}} \nu_{ij}^f \mu_i^{\text{u,PG}}\right), \quad j \in \mathcal{R}, \quad (10)$$

$$\kappa_j^b = \kappa_j^s \exp\left(\sum_{i \in \mathcal{S}} \nu_{ij}^b \mu_i^{\text{u,PG}}\right), \quad j \in \mathcal{R}, \quad (11)$$

which fulfill the classical relations  $\kappa_j^b = \kappa_j^f \exp\left(\sum_{i \in \mathcal{S}} (\nu_{ij}^f - \nu_{ij}^b) \mu_i^{\text{u,PG}}\right)$ . The relations (10) and (11) can then be used to estimate the symmetric constants  $\kappa_j^s$  from classical forward constants  $\kappa_j^f$  given by standard low pressure kinetics scheme.

Introducing the activities  $a_i = \exp(\mu_i - \mu_i^{\text{u,PG}})$ ,  $i \in \mathcal{S}$ , the generalized form of the rate of progress (9) can be written under the form of a generalized mass action law

$$\tau_j = \kappa_j^f \prod_{i \in \mathcal{S}} a_i^{\nu_{ij}^f} - \kappa_j^b \prod_{i \in \mathcal{S}} a_i^{\nu_{ij}^b}.$$

Under this form, we recover the general equilibrium condition

$$\kappa_j^{\text{eq}} = \kappa_j^f / \kappa_j^b = \prod_{i \in \mathcal{S}} (a_i^{\nu_{ij}^f - \nu_{ij}^b}),$$

which is then a direct consequence of the Marcelin expression (9).

The formulation of the reactions rate of progress presented here allow a natural introduction of nonideality effects in chemical kinetics. These effects do not reduce to an equilibrium displacement through a Le Chatellier's effect brought by density enhancement at high pressure and are equally and naturally distributed on forward and backward reactions. By comparing with perfect gas rate of progress, the influence of these effect have been found [14] to rise from a few percent at  $p = 100$  atm up to 25% at  $p = 1000$  atm.

The kinetic scheme used in this study is the one proposed by Ó Conaire *et al.* [56] as an improvement of the work of Mueller *et al.* [57] and is described in Table 1. Note that this scheme is used without the formation enthalpy modifications recommended by Ó Conaire.

## 2.5 Numerical method

The set of equation (1) (2) (3) and (4) is discretized by using finite difference and solved on self-adaptative grids with the aid of Newton's method [58]. To compute a flame structure from scratch, pseudo unsteady iterations are used to bring an initial guess into the convergence domain of steady Newton's iteration. The grid is statically iteratively refined by adding discretization points wherever the solution gradients are too roughly represented.

Once a flame structure is obtained, it may be used as a starting point to compute solutions branches depending on a parameter such as the strain rate  $\varepsilon$ . Branches are computed by means of continuation techniques [59] using global rezone adaptative gridding that generates smooth grids. The solution branches are locally reparameterized by the most sensitive solution component hence allowing the computation of turning points and insuring that the solution is changing smoothly.

The evaluation of fluid properties such as chemical production rate, thermodynamic properties and transport coefficient is obtained thanks to high pressure adapted version of the highly optimized thermochemistry and transport routines [60, 61, 62, 63, 64, 65]. The thermochemistry routines optimization lies in a systematic vectorization whereas the transport routines combine vectorization and the use of iterative method for the solving of the transport linear system.

In addition, the computation of the diffusion driving force  $d_i$ ,  $i \in \mathcal{S}$  use an efficient evaluation [14] of the fixed temperature gradient of dimensionless chemical potential  $(\mu_i)'_T$  which do not requires the evaluation of the partial derivatives with respect of the species molar fraction of this potential and a summation over the whole species set.

## 3 Pseudo vaporizing O<sub>2</sub>

We study in this section a transcritical O<sub>2</sub> pseudo vaporization layer, following the work of Pons *et al.* [11]. Such a phenomenom corresponds to the rapid yet continuous density variation of oxygen during

j	Reaction	$\mathfrak{A}_j$	$\mathfrak{b}_j$	$\mathfrak{C}_j$
1	$\text{H} + \text{O}_2 \rightleftharpoons \text{O} + \text{OH}$	$1.91 \times 10^{14}$	0.00	16.440
2	$\text{O} + \text{H}_2 \rightleftharpoons \text{H} + \text{OH}$	$5.08 \times 10^{14}$	2.67	6.292
3	$\text{OH} + \text{H}_2 \rightleftharpoons \text{H} + \text{H}_2\text{O}$	$2.16 \times 10^8$	1.51	3.430
4	$\text{O} + \text{H}_2\text{O} \rightleftharpoons \text{OH} + \text{OH}$	$2.97 \times 10^6$	2.02	13.400
5 <sup>a</sup>	$\text{H}_2 + \text{M} \rightleftharpoons \text{H} + \text{H} + \text{M}$	$4.57 \times 10^{19}$	-1.40	105.100
6 <sup>a</sup>	$\text{O} + \text{O} + \text{M} \rightleftharpoons \text{O}_2 + \text{M}$	$6.17 \times 10^{15}$	-0.50	0.000
7 <sup>a</sup>	$\text{O} + \text{H} + \text{M} \rightleftharpoons \text{OH} + \text{M}$	$4.72 \times 10^{18}$	-1.00	0.000
8 <sup>b</sup>	$\text{H} + \text{OH} + \text{M} \rightleftharpoons \text{H}_2\text{O} + \text{M}$	$4.50 \times 10^{22}$	-2.00	0.000
9 <sup>c,d</sup>	$\text{H} + \text{O}_2 + \text{M} \rightleftharpoons \text{HO}_2 + \text{M}$	$3.48 \times 10^{16}$	-0.41	-1.120
	$\text{H} + \text{O}_2 \rightleftharpoons \text{HO}_2$	$1.48 \times 10^{12}$	0.60	0.000
10	$\text{HO}_2 + \text{H} \rightleftharpoons \text{H}_2 + \text{O}_2$	$1.66 \times 10^{13}$	0.00	0.820
11	$\text{HO}_2 + \text{H} \rightleftharpoons \text{OH} + \text{OH}$	$7.08 \times 10^{13}$	0.00	0.300
12	$\text{HO}_2 + \text{O} \rightleftharpoons \text{OH} + \text{O}_2$	$3.25 \times 10^{13}$	0.00	0.000
13	$\text{HO}_2 + \text{OH} \rightleftharpoons \text{H}_2\text{O} + \text{O}_2$	$2.89 \times 10^{13}$	0.00	-0.500
14 <sup>f</sup>	$\text{HO}_2 + \text{HO}_2 \rightleftharpoons \text{H}_2\text{O}_2 + \text{O}_2$	$4.2 \times 10^{14}$	0.00	11.980
	$\text{HO}_2 + \text{HO}_2 \rightleftharpoons \text{H}_2\text{O}_2 + \text{O}_2$	$1.3 \times 10^{11}$	0.00	-1.629
15 <sup>a,e</sup>	$\text{H}_2\text{O}_2 + \text{M} \rightleftharpoons \text{OH} + \text{OH} + \text{M}$	$1.27 \times 10^{17}$	0.00	45.500
	$\text{H}_2\text{O}_2 \rightleftharpoons \text{OH} + \text{OH}$	$2.95 \times 10^{14}$	0.00	48.400
16	$\text{H}_2\text{O}_2 + \text{H} \rightleftharpoons \text{H}_2\text{O} + \text{OH}$	$2.41 \times 10^{13}$	0.00	3.970
17	$\text{H}_2\text{O}_2 + \text{H} \rightleftharpoons \text{H}_2 + \text{HO}_2$	$6.03 \times 10^{13}$	0.00	7.950
18	$\text{H}_2\text{O}_2 + \text{O} \rightleftharpoons \text{OH} + \text{HO}_2$	$9.55 \times 10^6$	2.00	3.970
19 <sup>f</sup>	$\text{H}_2\text{O}_2 + \text{OH} \rightleftharpoons \text{H}_2\text{O} + \text{HO}_2$	$1.00 \times 10^{12}$	0.00	0.000
	$\text{H}_2\text{O}_2 + \text{OH} \rightleftharpoons \text{H}_2\text{O} + \text{HO}_2$	$5.80 \times 10^{14}$	0.00	9.560

<sup>a</sup> Third body efficiency  $\text{H}_2\text{O} = 12.0$ ,  $\text{H}_2 = 2.5$

<sup>b</sup> Third body efficiency  $\text{H}_2\text{O} = 12.0$ ,  $\text{H}_2 = 0.73$

<sup>c</sup> Third body efficiency  $\text{H}_2\text{O} = 14.0$ ,  $\text{H}_2 = 1.3$

<sup>d</sup> Troe parameters:  $a = 0.5$ ,  $T^* = 1.0 \times 10^{30}$ ,  $T^{**} = 1.0 \times 10^{100}$ ,  $T^{***} = 1.0 \times 10^{-30}$

<sup>e</sup> Troe parameters:  $a = 0.5$ ,  $T^* = 1.0 \times 10^{30}$ ,  $T^{**}$  not used,  $T^{***} = 1.0 \times 10^{-30}$

Reaction 14 and 19 are expressed as the sum of two rate expressions.

Units are  $\text{cm}^3$ , mol, s, kcal, K

Table 1: Ó Conaire kinetic scheme for hydrogen combustion [56]

the heating process. The pseudo vaporization phenomenon is emblematic of high pressure running engines since the behaviour of the dense oxygen core differs dramatically between supercritical cases and subcritical cases.

### 3.1 Strained pseudo vaporizing layer

Injector devices used in cryogenic rocket engines are typically coaxial injectors for which the dense oxygen core is surrounded by a fast moving hydrogen jet. This geometry enhances the mixing of these two ergols and hence the combustion efficiency. As a consequence, oxygen pseudo vaporization arises in highly sheared mixing layers with high stretch rate. This layer is here represented by two impinging jets. One consists of dense oxygen at the low temperature of  $T^{\text{up}} = 100$  K and the other of oxygen already heated by combustion at the temperature  $T^{\text{do}} = 1000$  K. The mean pressure being fixed at  $p = 100$  atm, the oxygen is fully transcritical and no phase transition is expected.

The value of the strain rate  $\varepsilon$  is here taken equal to  $\varepsilon = 10000 \text{ s}^{-1}$  which is relevant of the conditions encountered in the wake of a rocket injector but its exact value is not fundamental since the equations (1), (2), (3) and (4) for non-reactive ( $\omega_i = 0$ ,  $i \in \mathcal{S}$ ) stretched structures yield solutions which are only dependent on  $\tilde{x} = x\sqrt{\varepsilon}$  as soon as the mass and energy fluxes can be written under the form of linear combination of  $x$  derivatives. The formulation of the equation governing these structures are detailed in Section 7

As defined by Pons [11], the pseudo vaporizing flux  $m^{\text{vp}} = \rho v(x^{\text{vp}})$  is used here with the pseudo vaporization location  $x^{\text{vp}}$  being set by  $T(x^{\text{vp}}) = T_{c,\text{O}_2}$ , where  $T_{c,\text{O}_2}$  is the critical temperature of oxygen. The choice to use the critical temperature of oxygen to determine pseudo vaporization is somewhat arbitrary and taking the temperature at which the specific heat at constant pressure of oxygen reaches

its maximum at a given pressure leads to similar results.

### 3.2 Reduced pseudo vaporizing mass transfer rate

By analogy with the expressions deduced from quasi stationary derivation of vaporizing processes, Yang [35] has proposed to express the pseudo vaporizing mass transfer rate per unit surface  $m^{\text{VP}}$  as a function of a Spalding-like parameter  $B_T$  given by

$$B_T = \frac{T^{\text{up}} - T_{c,\text{O}_2}}{T_{c,\text{O}_2} - T^{\text{do}}}.$$

Pons [11] has proposed the following relationship

$$m^{\text{VP}} \propto \ln(1 + B_T),$$

which is analog to the expression of stationary vaporization rates in the subcritical state. We define here a reduced pseudo vaporizing mass transfer rate per unit surface by

$$\tilde{m}^{\text{VP}} = \frac{m^{\text{VP}}}{\ln(1 + B_T)}.$$

Figure 1 presents the reduced vaporizing mass transfer rate per unit surface as a function of the Spalding-like parameter. In this figure, the Spalding-like parameter variation is obtained by altering the temperatures at both sides of the structure. The values of  $B_T$  displayed in Figure 1 correspond to  $1000 \text{ K} \leq T^{\text{up}} \leq 3495 \text{ K}$  for  $T^{\text{do}} = 100 \text{ K}$  and  $100 \text{ K} \leq T^{\text{do}} \leq 140,5 \text{ K}$  for  $T^{\text{up}} = 1000 \text{ K}$ . For such variation of the Spalding-like parameter, the reduced pseudo vaporization flux enhancement is comparable whether it is the cold temperature or the hot one which is increased. Moreover, for the whole  $B_T$  range and in the case of varying cold temperature, the relative variation of the reduced pseudo-vaporizing flux is less than 15% which confirms the correctness of the normalization.

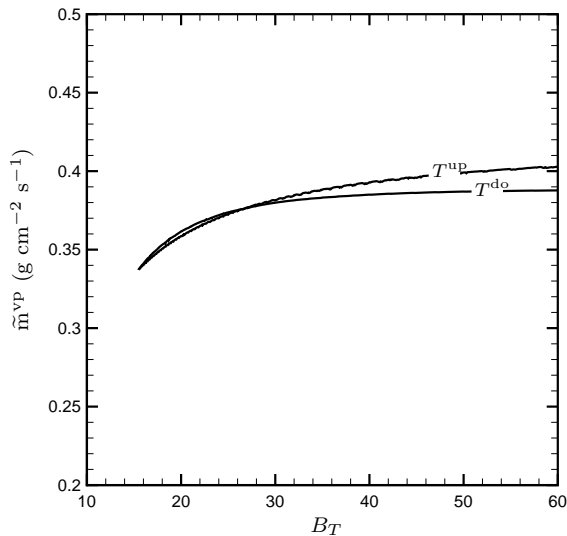


Figure 1: Reduced vaporizing flux as a function of the Spalding-like parameter

### 3.3 Sensitivity analysis

We study in this section the influence of high pressure transport models on the reduced pseudo-vaporizing mass transfer rate. The stretched structure being composed of an unique species, transport phenomena reduce to heat conduction and viscosity. Reduced pseudo-vaporizing mass transfer rates are computed for four different couples of transport coefficients which are the thermal conductivity and the shear viscosity. Figure 2 displays the evaluated reduced vaporizing mass transfer rate as a function of the  $T^{\text{do}}$  temperature. Solid line represents the reduced vaporizing mass transfer rate computed in the case the two transport coefficients are evaluated using high density correlation, hence

designed as  $(\lambda, \eta)$ . The line bearing diamonds  $\diamond$  represents the case the two transport coefficients are evaluated using results of the kinetic theory of diluted gases, hence  $(\lambda^{\text{dil}}, \eta^{\text{dil}})$ . The two remaining lines represent hybrid formulation respectively  $(\lambda, \eta^{\text{dil}})$  for the  $\nabla$  bearing line and  $(\lambda^{\text{dil}}, \eta)$  for the  $\square$  bearing one. For all modelizations, the reduced pseudo vaporizing mass transfer rate  $\tilde{m}^{\text{VP}}$  diverges for  $T^{\text{do}} \rightarrow T_{c, \text{O}_2} = 154, 58 \text{ K}$ , which corresponds to the fact that the pseudo-vaporizing interface is then rejected at  $x = -\infty$ . The influence of transport coefficients is rather complex but it seems that the weakening of thermal conductivity through the use of dilute formulations enhances the pseudo-vaporizing mass transfer rate. As expected, the influence of thermal conductivity weakens when the pseudo vaporizing interface is rejected toward  $x = -\infty$ . For the shear viscosity, its influence seems to vary depending on the injection temperature, enhancing the pseudovaporization for low injection temperature and reducing it at higher temperature.

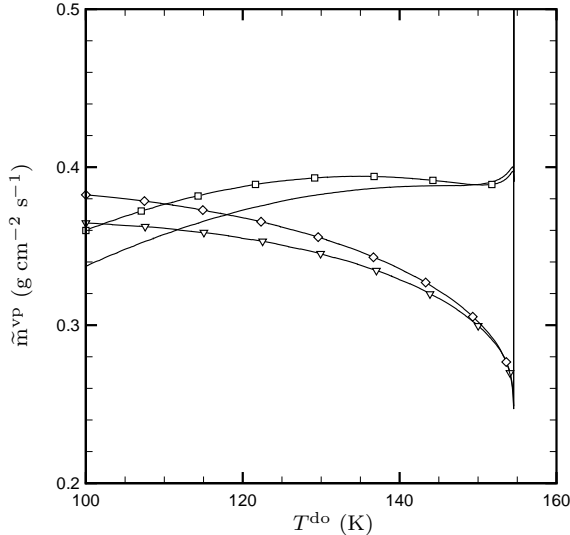


Figure 2: Reduced vaporizing flux as a function of  $T^{\text{do}}$  for varied transport modelization. —:  $(\lambda, \eta)$ ,  $\diamond$ :  $(\lambda^{\text{dil}}, \eta^{\text{dil}})$ ,  $\nabla$ :  $(\lambda, \eta^{\text{dil}})$ ,  $\square$ :  $(\lambda^{\text{dil}}, \eta)$

Nevertheless, with an eye towards subgrid models required for Large Eddy Simulations, the unavoidable errors made in averaging every turbulent structures in a single equivalent stretched structure being of a greater order, the relationship proposed by Pons [11] seems reasonably accurate.

## 4 H<sub>2</sub>-O<sub>2</sub> mixing layer

In this section, we investigate a mixing layer between cold oxygen and hydrogen at a pressure  $p = 100 \text{ atm}$ . This mixing layer is represented by a non-reactive stretched structure separating two impinging flow at temperature  $T = 150 \text{ K}$ . The value of the strain rate used here is  $\varepsilon = 10000 \text{ s}^{-1}$ , but as already noted for the O<sub>2</sub> pseudo vaporizing structure, the solution can be extended by similarity to any strain rate  $\varepsilon$ . This kind of structure is likely to appear in the wake of rocket engine injectors in the case of local flame quenching. The temperature of both injected oxygen and hydrogen are taken equal here for the sake of simplicity and slightly higher than the predicted thermodynamics stability of H<sub>2</sub>-O<sub>2</sub> mixtures which is around  $T = 140 \text{ K}$  as evaluated for instance with the SRK equation of state [14]. The two fluids are then expected to be weakly miscible one into another and we demonstrate here the capability of transport models based on thermodynamical consideration —such as the one described in Section 2.3— to grasp this lack of miscibility. These nonideal effects are out of reach of ideal transport models which may indeed lead to thermodynamically non-admissible states inside the mixing layer.

### 4.1 Structure of the mixing layer

Figure 3 presents the evolution of the density through the mixing layer for nonideal diffusion driving forces and ideal diffusion driving forces respectively. The density of hydrogen, coming from the left, is

about  $0.0154 \text{ g}\cdot\text{cm}^{-3}$  at  $T = 150 \text{ K}$  and  $p = 100 \text{ atm}$  and the density of oxygen rises up to  $0.768 \text{ g}\cdot\text{cm}^{-3}$ . For the mixing layer computed using the nonideal diffusion driving forces, the density gradients are much steeper than the ones observed with the ideal diffusion driving forces evaluation. In this case, the density curve presents here a nearly vertical tangent which tends to resemble the infinite density derivative existing at the interface between two unmiscible fluids. On the contrary, for the ideal model, the density gradients are much weaker and the density profile shows several inflection points.

In addition, as presented on Figure 4, the temperature does not stay uniform in the mixing layer although both fluids are injected at  $T = 150 \text{ K}$ . These perturbations may be explained thanks to two physically distinct effects. Combining the species and energy conservation (3) (4) in this two-species inert context, we first write the following equation for temperature

$$(\rho v c_p + \sum_{i \in \mathcal{S}} \mathcal{F}_i c_{p,i}) T' - (\hat{\lambda} T')' = - \left( \frac{\rho R T}{\bar{m}} (\theta_{\text{H}_2} d_{\text{H}_2} - \theta_{\text{O}_2} d_{\text{O}_2}) \right)' + \sum_{i,j \in \mathcal{S}} \mathcal{F}_i h_{ij} Y_j',$$

where  $c_p$  is the mean specific heat of the mixture and  $h_{ij} = \partial h_i / \partial Y_j = \partial h_j / \partial Y_i$  are the enthalpy cross derivatives. The two terms on the right side may be interpreted as temperature source terms. The first is related to Dufour's effect and the second is a nonideal thermodynamical effect related to the fact that, for real gases, the cross enthalpy derivatives  $h_{ij}$  are generally non zero. In the computed  $\text{H}_2\text{-O}_2$  mixing layer this thermodynamical effect dominates the Dufour effect and leads to lower temperatures in the hydrogen-rich side of the layer and higher temperatures in the oxygen-rich side.

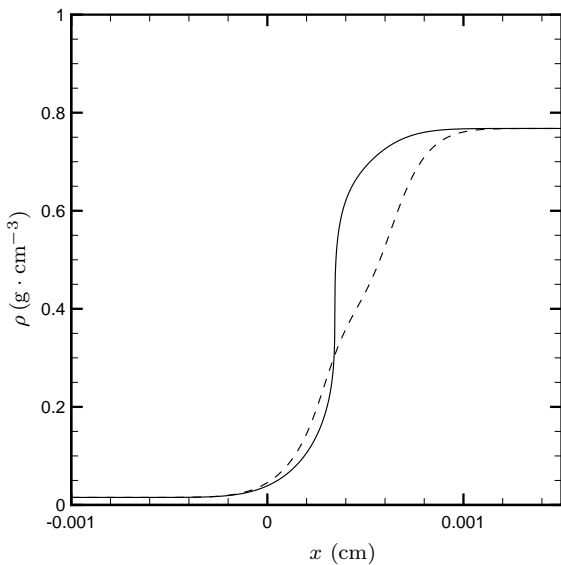


Figure 3: Density evolution in the cold  $\text{H}_2\text{-O}_2$  mixing layer. (—) :  $X_i(\mu_i)'_T$ , (- - -) :  $X_i'$

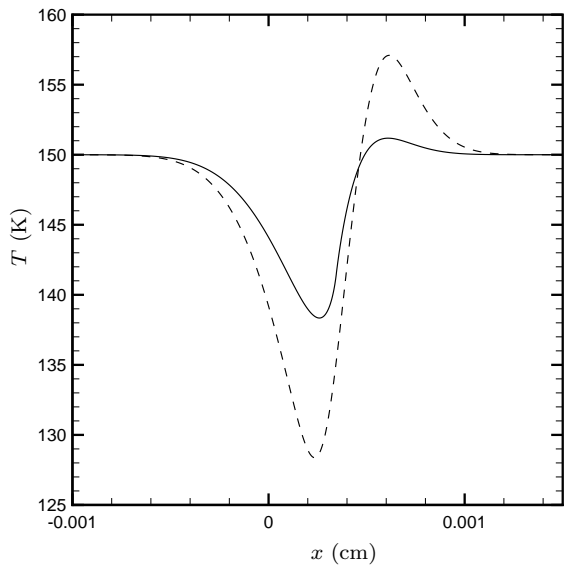


Figure 4: Temperature evolution in the cold  $\text{H}_2\text{-O}_2$  mixing layer. (—) :  $X_i(\mu_i)'_T$ , (- - -) :  $X_i'$

We note that density gradients are steeper with nonideal transport. This effect is the consequence of the counter-diffusion brought by the nonideal part of the diffusion driving forces  $X_i(\mu_i^{\text{sm}})'_T$  as shown in Figures 5 and 6 where the two part of these forces are independently plotted. These figures underline the dramatic influence of the nonideal part of the diffusion driving force which hinders the natural diffusion. This nonideal part of the diffusion driving force is responsible of an anti-diffusion flux which counter-balance the classical mass flux driven by the mole fraction gradients. This anti-diffusion flux is localized in the vicinity of the locus of higher density gradient and the magnitude of the corresponding diffusion driving force peaks to  $41500 \text{ cm}^{-1}$ . The consequences of this anti-diffusion flux is that the two impinging jets are relatively preserved in what concerns the mixture composition, which lead to the appearance of a quasi-interface. Such a phenomenon is to be expected in the neighborhood of the thermodynamic chemical stability limit where phase separation occurs.

## 4.2 Thermodynamic stability

Using SRK thermodynamics, the critical line of  $\text{H}_2\text{-O}_2$  mixtures lies for the pressure  $p = 100 \text{ atm}$  at a temperature  $T = 141 \text{ K}$ . At this pressure,  $\text{H}_2\text{-O}_2$  mixtures may become unstable for temperatures lower

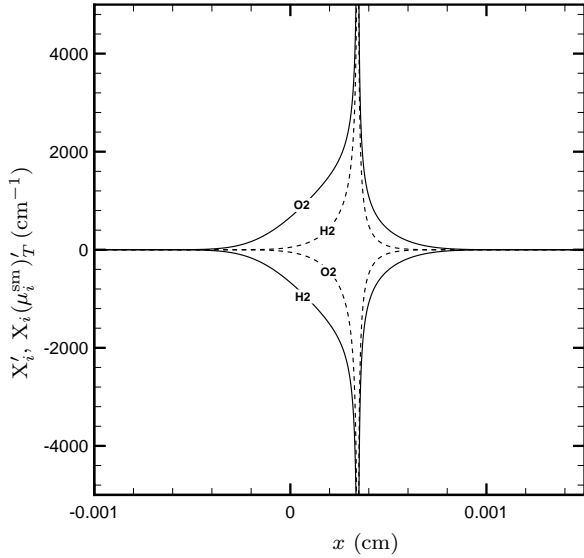


Figure 5: Diffusion driving forces in the cold H<sub>2</sub>-O<sub>2</sub> mixing layer. (—) :  $X'_i$ , (---) :  $X_i(\mu_i^{\text{sm}})'_T$

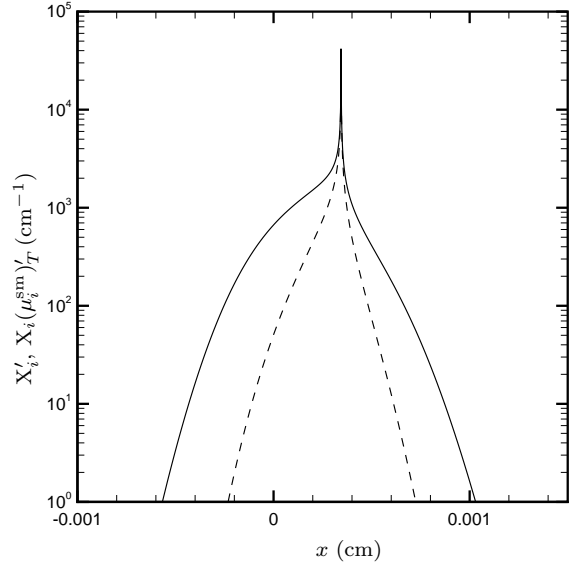


Figure 6: Detail of the magnitude of the distinct part of the diffusion layer driving forces in the cold H<sub>2</sub>-O<sub>2</sub> mixing layer. (—) :  $X'_{\text{O}_2}$ , (---) :  $X_{\text{H}_2}(\mu_{\text{H}_2}^{\text{sm}})'_T$

that the critical line temperature. As shown in Figure 4, the computed mixing layer structures present thermodynamical states with temperatures lower than  $T = 141$  K and it is then necessary to check their thermodynamical stability. In Figure 7 are plotted the varied thermodynamical states encountered in the H<sub>2</sub>-O<sub>2</sub> mixing layers in a mixture-temperature diagram along with the stability limit computed for SRK thermodynamics. As it appears, when the ideal diffusion driving force model is used, some of the encountered thermodynamical states are under the stability limit curve and thus unphysical. On the contrary, the full high pressure model manage to avoid intrusion inside the non-admissibility domain by inflecting the composition-temperature curve and thus introducing steep density gradients.

The nonideal transport model is consistant with nonideal thermodynamics in the sense that unconditionally unstable thermodynamical states cannot be obtained through a molecular transport process. Indeed the nonideal transport model introduces diffusion driving forces based on entropy derivatives with respect to the component mass and the energy allowing the model to grasp stability properties which are related to the matrices.

## 5 Diffusion flame structure

In this section, we present some diffusion flames structures relevant of combustion phenomena arising inside a cryogenic rocket engine.

### 5.1 H<sub>2</sub>-O<sub>2</sub> transcritical flame

We consider an H<sub>2</sub>-O<sub>2</sub> diffusion flame at pressure  $p = 100$  atm and injection temperatures  $T^{\text{up}} = 300$  K and  $T^{\text{do}} = 100$  K respectively. This kind of flames can be found in the vicinity of cryogenic rocket engine injectors where flames stabilize between the dense oxygen core and the preheated hydrogen coflow.

We describe here the structure of the H<sub>2</sub>-O<sub>2</sub> diffusion flame computed for an  $\varepsilon = 10000 \text{ s}^{-1}$  strain rate. An important feature of this flame structure is the large densities encountered in the oxygen injection for positive  $x$ . This density rise indeed as high as  $1.12 \text{ g}\cdot\text{cm}^{-3}$  which are approaching densities of liquid oxygen. The maximal temperature  $T^{\text{max}} = 3747$  K is to be found in the vicinity of  $x = 19.6 \mu\text{m}$ , the crossing position of the fuel and oxydant mole fraction where  $X_{\text{H}_2, \text{O}_2} = 0.078$ .

The whole flame structure is around  $50 \mu\text{m}$  wide and the two side of the flame are quite different. On the O<sub>2</sub> side, the heavier radical are to be found with early formation of H<sub>2</sub>O<sub>2</sub> radicals through reaction 15. Note that the fuel H<sub>2</sub> penetrate the O<sub>2</sub> dense core deeper than every other component even than the combustion product H<sub>2</sub>O. The latter point can be explained by considering that hydrogen

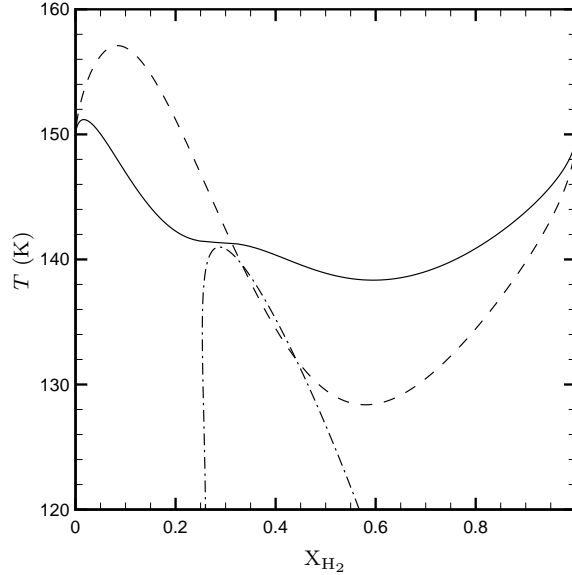


Figure 7: Thermodynamical states encountered in the cold  $\text{H}_2\text{-O}_2$  mixing layer. (—) :  $X_i(\mu_i^{\text{sm}})'_T$ , (- - -) :  $X'_i$ , (- · -) : stability limit

does not react with oxygen at these low temperature and that its diffusivity as a small molecule is greater than the one of water. In the same way in the  $\text{H}_2$  side, the H radical diffuse faster than the  $\text{H}_2\text{O}$  molecule and thus goes further in the impinging  $\text{H}_2$  jet.

Whereas in the cold  $\text{H}_2\text{-O}_2$  mixing layer the diffusion driving force model was of the greatest influence on the stretched structure, it does not seem to bear the same influence in this case. Indeed using the ideal diffusion driving forces  $X'_i$ ,  $i \in \mathcal{S}$  does not change significantly the flame structure and the radicals profile. The only influence reduces to a slightly better diffusivity of  $\text{H}_2\text{O}$  inside the dense  $\text{O}_2$  core and the smoothing of a kind of bump in the  $\text{O}_2$  mole fraction profile. This bump is due to a weak nonideal anti-diffusion effect on the edge of the dense core which induced steep initial  $X_{\text{O}_2}$  gradients to counterbalance this effect. This bump is quite small and thus can not be seen on Figure 8, but its effect on the  $X'_{\text{O}_2}$  is made clear on Figure 9 on which are plotted the contributions  $X_{\text{O}_2}$  and  $X_{\text{O}_2}(\mu_{\text{O}_2}^{\text{sm}})'_T$  to  $d_{\text{O}_2}$ .

The nonideal part of the diffusion force  $X_{\text{O}_2}(\mu_{\text{O}_2}^{\text{sm}})'_T$  plays a role in a very narrow sheet around the high density gradient zone. Its influence is to prevent diffusion of  $\text{O}_2$  molecules from the dense core to the flame. As a consequence, the mole fraction gradient profile presents a kind of horn in this steep density gradient region, horn that can be obliterated by neglecting the nonideal diffusion. Taking into account the thermal diffusion does not modify this conclusion as its own influence is mainly located inside the flame and not in the pseudo-interface region.

The nonideal transport influence on the  $\text{O}_2$  pseudo-vaporizing mass transfer rate is thus weak compared to the thermal effects. The multi-species flame sheet is separated from the pure species dense  $\text{O}_2$  core by this thermally controlled pseudo-vaporizing front, justifying subgrid models based on pseudo-vaporizing interface consideration [66].

## 5.2 ( $\text{H}_2+\text{H}_2\text{O}$ )- $\text{O}_2$ diffusion flames

An other kind of diffusion flame structure of great interest in cryogenic combustion is constituted by a cold  $\text{O}_2$  jet impinging on a hot mixture of burnt gases. Most cryogenic engines running at high fuel ratio, these burnt gases may contain enough residual hydrogen to allow inflammation of the oxydant. This kind of structure may develop around a dense  $\text{O}_2$  cluster ripped of the main core by turbulence and thrown in the middle of already burnt gases.

In this section we modelize the burnt gases as a mixture of  $\text{H}_2$  and  $\text{H}_2\text{O}$  at the temperature of  $T^{\text{do}} = 1000$  K. The  $\text{O}_2$  dense core is once again represented by an impinging jet at temperature  $T^{\text{up}} = 100$  K, hence implying transcritical behaviour of the oxydizer. The pressure of the flame is taken equal to  $p = 100$  atm. We consider a global oxydizer to fuel mixture ratio of 1.5 relevant of gas generator condition, that is to say extremely rich in hydrogen. The burnt gases are thus represented

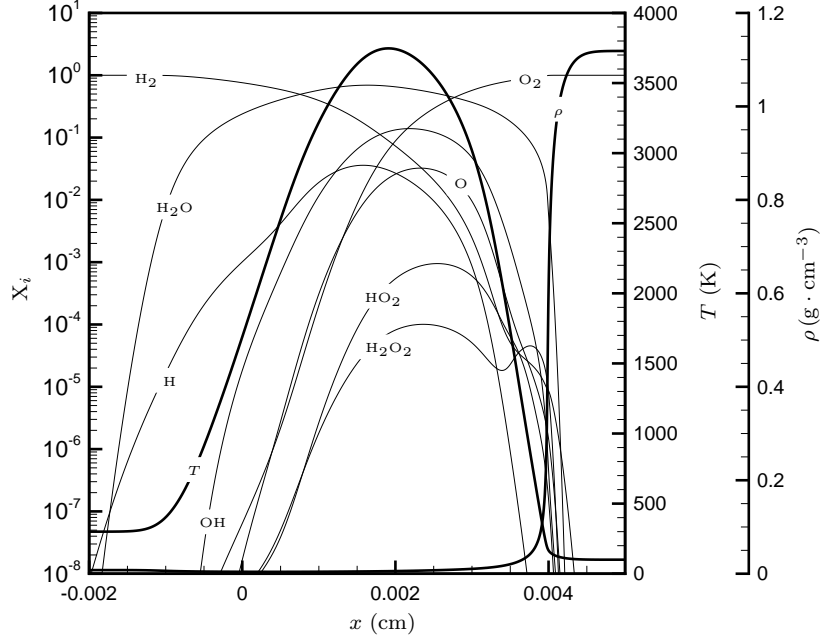


Figure 8: Structure of a counterflow  $\text{H}_2\text{-O}_2$  diffusion flame, with  $T^{\text{up}} = 100$  K,  $Y_{\text{O}_2}^{\text{up}} = 1$ ,  $T^{\text{do}} = 300$  K,  $Y_{\text{H}_2}^{\text{do}} = 100$  K,  $\varepsilon = 10000$   $\text{s}^{-1}$

by a  $\text{H}_2\text{-H}_2\text{O}$  mixture with  $X_{\text{H}_2} = 0.8077$  and  $X_{\text{H}_2\text{O}} = 0.1923$ .

The flame structure is quite similar to the  $\text{H}_2\text{-O}_2$  diffusion flame, especially the right side near the  $\text{O}_2$  dense core. The width of the structure is quite the same but the whole structure is shifted left toward the stagnation point. Maximal temperature is slightly lower than in the previous case with  $T^{\text{max}} = 3633$  K, and molar fraction of  $\text{O}_2$  and  $\text{H}_2$  at crossing point is  $X_{\text{H}_2,\text{O}_2} = 0.07$ . The main differences lie in the enhanced diffusivities in hot burnt gases allowing radicals  $\text{H}$  and  $\text{OH}$  to crawl further inside the fuel jet.

## 6 Partially premixed flame

In this section, we study partially premixed  $\text{H}_2\text{-O}_2$  flames. These flames are established between a mixture of fuel and oxydizer and a pure oxydizer or fuel. This kind of configuration may occur in turbulent flows following local quenching which allows the fuel to mix with the oxydizer and reignition. In this study, we focus on the case in which the pure compound is cold oxygen in transcritical state.

In Figure 11 is presented the structure of a flame established between an hydrogen-rich mixture and a dense oxygen core. The pressure of the flame is set to  $p = 100$  atm and the temperature of the pure oxygen jet is fixed at  $T^{\text{up}} = 100$  K. For the hydrogen-rich mixture, we consider an isenthalpic mixing of  $\text{H}_2$  at  $T = 300$  K and  $\text{O}_2$  at  $T = 100$  K in a mixture ratio of 1.5, thus obtaining the following conditions:  $T^{\text{do}} = 263.35$  K and  $X_{\text{H}_2}^{\text{do}} = 0.9123$  and  $Y_{\text{O}_2}^{\text{do}} = 0.0877$ .

The side of the flame located near the oxygen injection is similar to the previously calculated diffusion flame, whereas the other side shows an independant reaction zone with heavy radicals  $\text{HO}_2$  and  $\text{H}_2\text{O}_2$  peaks located at  $x = -0.002$  cm. These peaks are soon followed by a steep increase of light radicals such as  $\text{O}$ ,  $\text{OH}$  and  $\text{H}$  and a weak inflection of the temperature profile. The radicals  $\text{O}$ ,  $\text{H}$ ,  $\text{OH}$ ,  $\text{HO}_2$ ,  $\text{H}_2\text{O}_2$  and species  $\text{O}_2$  mole fraction profiles presents a local minimum in the middle of the flame as the burnt premixed gases approach their thermodynamic equilibrium which is disturbed by the incoming of fresh  $\text{O}_2$  from the dense  $\text{O}_2$  injection. At the strain rate of  $\varepsilon = 10000$   $\text{s}^{-1}$  used here, the two distincts reaction zones are located close one to another and thus influence each other. This influence is weakened when these reaction zones are far apart.

In a first order analysis, the location  $x_f$  of the premixed reacting zone is given by the relation  $x_f \propto -v_f/\varepsilon$ , where  $v_f$  is the laminar flame speed in the mixture and where the proportionality coefficient is the ratio of the square roots of injected densities  $\sqrt{\rho^{\text{do}}/\rho^{\text{up}}}$ . In order to induce a displacement of the premixed zone to the left, one can then manage to increase the laminar flame speed  $v_f$  or reduce

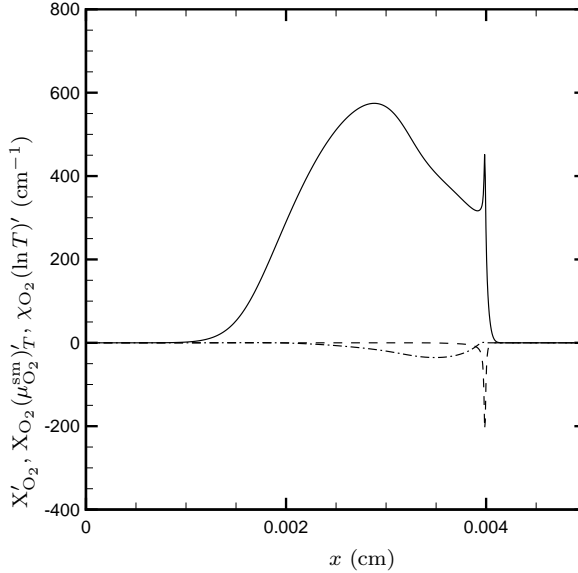


Figure 9: Contribution to the  $O_2$  related diffusion driving force. (—):  $X'_{O_2}$ , (- - -):  $X_{O_2}(\mu_{O_2}^{sm})'_T$ , (- · -):  $\chi_{O_2}(\ln T)'$

the strain rate  $\varepsilon$ .

The laminar flame speed can be increased by higher mixture temperature. Figure 12 shows a premixed flame structure computed for  $T^{do} = 1000$  K. The premixed reaction zone is located at  $x = -0.022$  cm and the burnt gases mixture has enough time to reach an equilibrium state before encountering the influence of the dense  $O_2$  core. The diffusion reacting zone is not influenced by this changes in the hydrogenated injection, the location of steeper density gradient being the same as in the case  $T^{up} = 300$  K and the mole fraction profiles being equivalent with the exception of the light radical ones which does not fall back to zero on the left side of this reacting zone but instead reaching the equilibrium values of the premixed burnt gases.

In order to obtain a displacement of the premixed burning zone, one may also reduce the stretch rate  $\varepsilon$  to allow the premixed-like flame to crawl further ahead the  $H_2$ - $O_2$  mixture. The figure 13 shows the structure obtained for a stretch rate  $\varepsilon = 200$   $s^{-1}$ . As in the hot  $H_2$ - $O_2$  mixture case, the fluid has enough time to reach thermodynamical equilibrium between the two reaction zones. This equilibrium presents lower temperature and as a consequence lower radical concentration. The diffusion reaction zone presents, taken into account the usual  $\sqrt{\varepsilon}$  similarity, the same features as the case with  $T^{up} = 300$  K and  $\varepsilon = 10000$   $s^{-1}$  except that the maximal temperature is here 10 K higher than in the previous case and that the  $H_2O_2$  secondary peak is somewhat lower than the previous one.

## 7 Extinction limits of $(H_2+H_2O)$ - $O_2$ flames

We investigate in this section the dilution extinction limits and the strain extinction limits of  $(H_2+H_2O)$ - $O_2$  diffusion flames. We also determine the flammability limits of  $H_2$ - $O_2$  mixtures in a stretched context.

### 7.1 Dilution extinction limit

Extinction of flame arising between transcritical oxygen and hydrogenated combustion product can be obtained by lowering the  $H_2$  concentration. The study is performed at the fixed stretch rates  $\varepsilon = 10^2, 10^3, 10^4, 10^5, 10^6$  and  $10^7$   $s^{-1}$ .

The hydrogenated combustion products are represented by  $H_2$ - $H_2O$  mixtures at a fixed temperature  $T^{do} = 1000$  K. The flame pressure is set to  $p = 100$  atm and the temperature of the injected  $O_2$   $T^{up} = 100$  K is low enough for the latter to be considered transcritical. The purpose is here to compute the family of solution obtained by varying the hydrogen mole fraction  $X_{H_2}^{do}$  in the hot impinging jet.

Figure 14 shows the maximal temperature reached in the flame structure as a function of the hydrogen molar fraction  $X_{H_2}^{do}$  in the hydrogenated combustion products. For a given mixture ratio, there may exist up to three different solutions leading to distinct maximal temperature. For instance

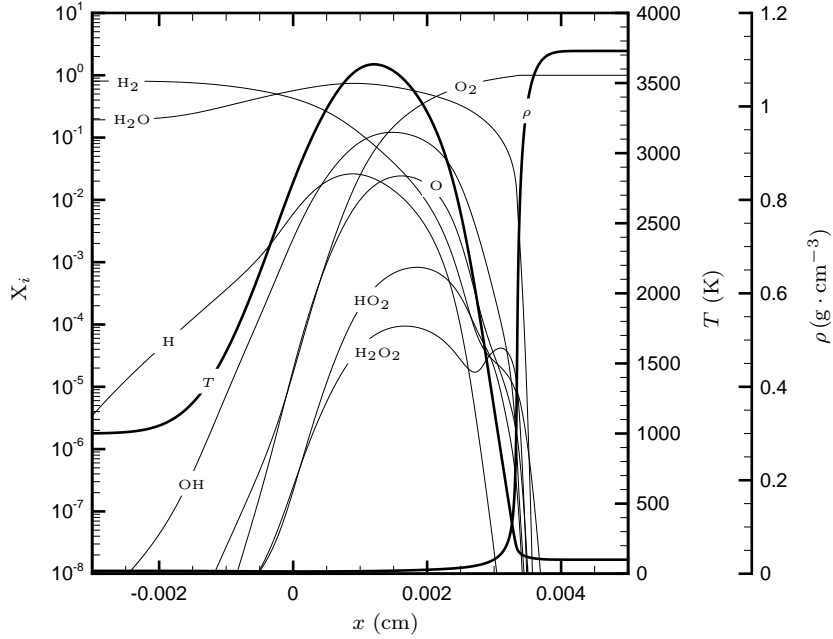


Figure 10: Structure of a counterflow (H<sub>2</sub>+H<sub>2</sub>O)-O<sub>2</sub> diffusion flame, with  $T^{\text{up}} = 100$  K,  $X_{\text{O}_2}^{\text{up}} = 1$ ,  $T^{\text{do}} = 1000$  K,  $X_{\text{H}_2}^{\text{do}} = 0.8077$ ,  $X_{\text{O}_2}^{\text{do}} = 0.1923$ ,  $\varepsilon = 10000$  s<sup>-1</sup>

for a stretch rate fixed at  $\varepsilon = 10^2$  s<sup>-1</sup> the solution curve is S-shaped. Starting from an extinguished solution with  $X_{\text{H}_2}^{\text{do}} = 0$  and  $T^{\text{max}} = 1000$  K, one can reach by increasing continuously the mixture ratio the ignition point located at  $X_{\text{H}_2}^{\text{do}} = 0.289$  where the solution undergo a transition toward the burning solution for which  $T^{\text{max}} = 2572$  K. Reducing then continuously the hydrogen mole fraction would lead to reach the extinction point located at  $X_{\text{H}_2}^{\text{do}} = 0.073$  for which the flame extinguish abruptly. The middle branch of the S-shaped curve is physically unstable and none of its solution is encountered in the real field. For higher stretch rate, the upper branch and the lower branch of the S, respectively the burning branch and the extinguished branch, are not connected anymore, leading to C-shaped curves. In this study we chose not to compute the always existing extinguished solutions which are of limited interest and only the burning and the unstable branch are plotted on Figure 14.

For H<sub>2</sub>-rich combustion product, the characteristic chemical time is small and the flame structure dependence with respect to the stretch rate reduces to a similarity deformation up to very large stretch rate. Indeed for pure reactant diffusion flame, the maximal flame temperature  $T^{\text{max}} = 3822$  K is stretch rate independant up to  $\varepsilon \simeq 10^7$  s<sup>-1</sup>. The lower the hydrogen mole fraction, the greater the chemical time is and the sooner appear influence of the stretch rate parameter. Table 2 gives the extinction limit in term of injected hydrogen mole fraction for varied stretch rate.

$\varepsilon$ (s <sup>-1</sup> )	10 <sup>2</sup>	10 <sup>3</sup>	10 <sup>4</sup>	10 <sup>5</sup>	10 <sup>6</sup>	10 <sup>7</sup>
$X_{\text{H}_2}^{\text{ext}}$	0.073	0.119	0.180	0.267	0.437	0.959

Table 2: Extinction limit of (H<sub>2</sub>+H<sub>2</sub>O)-O<sub>2</sub> flames

Combustion models based on stretched flames use global quantities to describe the flame behaviour. One of these quantities is the heat release per unit flame surface  $\omega_h$  defined as

$$\omega_h = - \int_{-\infty}^{+\infty} \sum_{i \in \mathcal{S}} h_i m_i \omega_i dx,$$

and appear as a source term in the temperature equation for turbulent combustion models. Under the infinitely fast chemistry assumption, the consumption rate of reactant is similar with respect to the square root of the strain rate  $\sqrt{\varepsilon}$  and so is the heat release. It is then interesting to define a reduced heat release  $\omega_h/\sqrt{\varepsilon}$  per unit flame surface to evaluate the validity of this fast chemistry assumption.

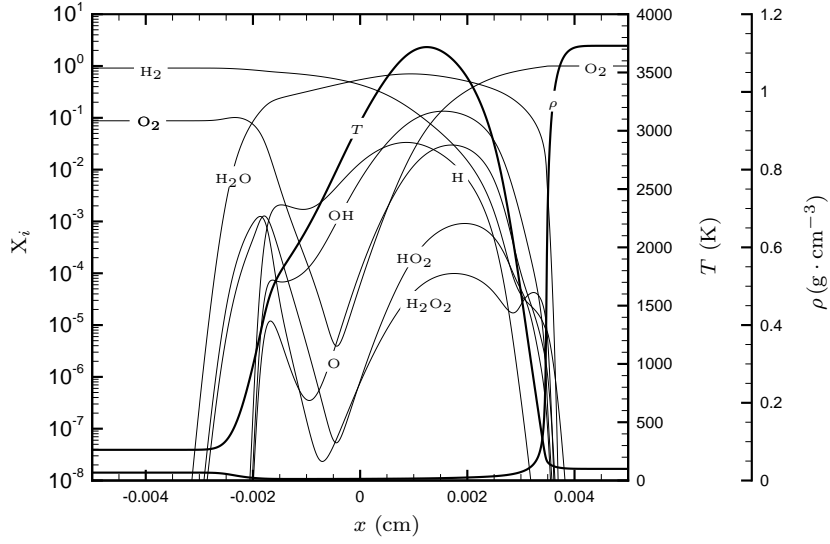


Figure 11: Structure of a counterflow partially premixed flame, with  $T^{\text{up}} = 100$  K,  $T^{\text{do}} = 263.35$  K,  $X_{\text{O}_2}^{\text{up}} = 1$ ,  $X_{\text{O}_2}^{\text{do}} = 0.0877$ ,  $X_{\text{H}_2}^{\text{do}} = 0.9123$ ,  $\varepsilon = 10000$  s $^{-1}$

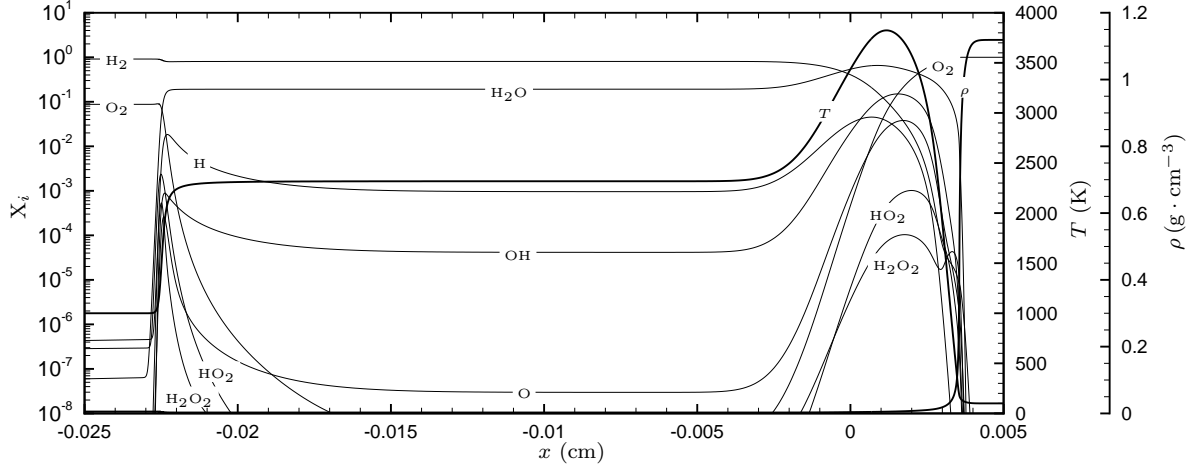


Figure 12: Structure of a counterflow partially premixed flame, with  $T^{\text{up}} = 100$  K,  $T^{\text{do}} = 1000$  K,  $X_{\text{O}_2}^{\text{up}} = 1$ ,  $X_{\text{O}_2}^{\text{do}} = 0.0877$ ,  $X_{\text{H}_2}^{\text{do}} = 0.9123$ ,  $\varepsilon = 10000$  s $^{-1}$

Figure 15 shows the reduced heat release per unit of flame surface for varied strain rate. This quantity appear to be a function of the hydrogen mole fraction only over a wide range of mixture ratio and of stretch rate. The influence of the stretch rate parameter is only sensible in the vicinity of extinction limit and for large values such as  $\varepsilon \geq 10^5$ .

## 7.2 Stretch extinction limit

In the case of hydrogen combustion, fast chemical kinetics leads to very high extinction stretch rate for H $_2$ -rich fuel jets. For the set of equations (1), (2), (3) and (4), the continuation procedure used to investigate extinction limits captures the fast-chemistry similarity deformation of the flame with respect to the stretch rate.

The molecular transport flux being expressed as sum of transport coefficient-pondered gradients, it is possible to rewrite the conservation equation set under a form which erase the similar deformation and thus ease the reaching of extinction limits. Indeed, denoting  $\tilde{x} = x\sqrt{\varepsilon}$  and  $\tilde{v} = v/\sqrt{\varepsilon}$  these equations

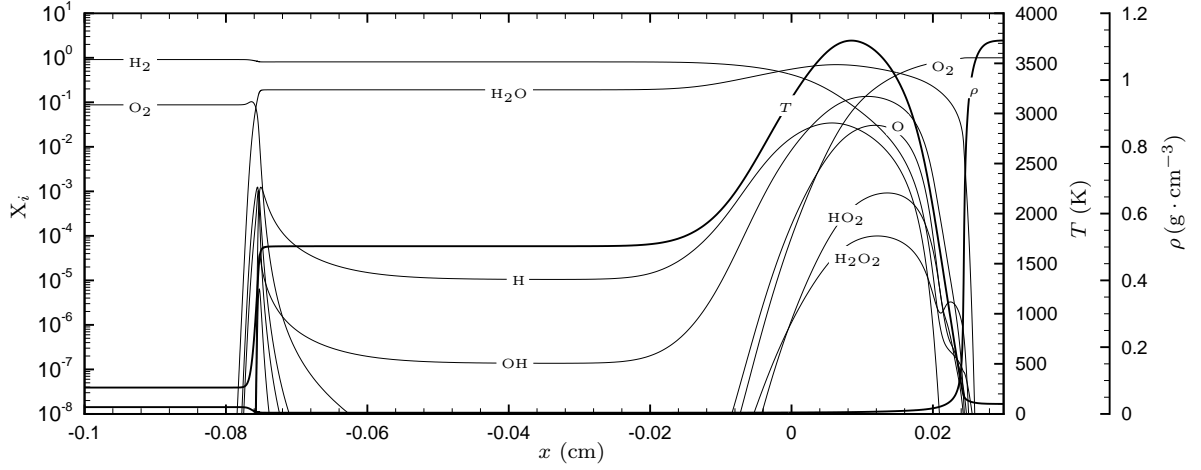


Figure 13: Structure of a counterflow partially premixed flame, with  $T^{\text{up}} = 100$  K,  $T^{\text{do}} = 263.35$  K,  $X_{\text{O}_2}^{\text{up}} = 1$ ,  $X_{\text{O}_2}^{\text{do}} = 0.0877$ ,  $X_{\text{H}_2}^{\text{do}} = 0.9123$ ,  $\varepsilon = 200$  s $^{-1}$

now read

$$\begin{aligned}
 \rho \tilde{u} + (\rho \tilde{v})' &= 0, \\
 \rho \tilde{v} \tilde{u}' + \rho \tilde{u}^2 - \rho^{\text{up}} - (\eta \tilde{u}')' &= 0, \\
 \rho \tilde{v} Y_i' + \left( \sum_{j \in \mathcal{S}} L_{ij} \left( -\frac{g_j}{T} \right)' + L_{iq} \left( \frac{1}{T} \right)' \right)' &= \frac{m_i \omega_i}{\varepsilon}, \quad i \in \mathcal{S}, \\
 \rho \tilde{v} h' + \left( \sum_{j \in \mathcal{S}} L_{qj} \left( -\frac{g_j}{T} \right)' + L_{qq} \left( \frac{1}{T} \right)' \right)' &= 0,
 \end{aligned}$$

where  $'$  now denotes the derivation with respect to the reduced normal coordinate  $\tilde{x}$ . Under this form, the action of the stretch rate upon the similarity-corrected structure reduces to a modulation of the chemical source terms.

The stretch-related variable used in this study by the continuation solver is the parameter  $1/\varepsilon$ . In order to explore the whole range of stretch, this parameter will change of a few order of magnitude during the continuation procedure. The continuation procedure used here performs a sensitivity analysis to select the most relevant variable as continuation parameter [59]. A fixed scaling for the stretch-related parameter  $1/\varepsilon$  can artificially enhance or reduce the evaluated sensitivity with respect to this parameter and lead to suboptimal choices for the continuation parameter. In this study we use a dynamic scaling procedure insuring that the scaled stretch-related parameter is always of magnitude unity.

The figure 16 shows the maximal temperature  $T^{\text{max}}$  reached by counterflow flames for combustion product mixture ratio given by  $X_{\text{H}_2} = 0.1, 0.2, 0.3, 0.4, 0.5, 0.6, 0.7, 0.8, 0.9$ , and  $1.0$ . As expected, the maximal temperature is relatively independant of the stretch rate for low values of the latter.

The solution curves seems to be classically S-shaped but, albeit not apparent on the figure, some of the curves' extinguished and burning branch are no longer connected. In fact for medium mixture ratio, namely  $X_{\text{H}_2} = 0.8, 0.7, 0.6, 0.5, 0.4$ , the unstable branch possess flame structures containing thermodynamically unstable state. These unphysical solutions are typically found for stretch rate around  $10^2 \leq \varepsilon \leq 10^3$  which are great enough to weaken the chemistry and allow diffusion of water and hydrogen in the dense  $\text{O}_2$  jet.

Figure 17 represent the reduced heat release per unit of flame surface as a function of the stretch rate. The lack of dependence with respect of the stretch rate  $\varepsilon$  for the low values is once again apparent and the dispersion in term of heat release allows to point out the fact that some of the curves finishes on the unstable branch as evoked before. The extinguished branch coincide here with the abscisse axis since no chemical phenomenom occurs when the flamùe is not burning.

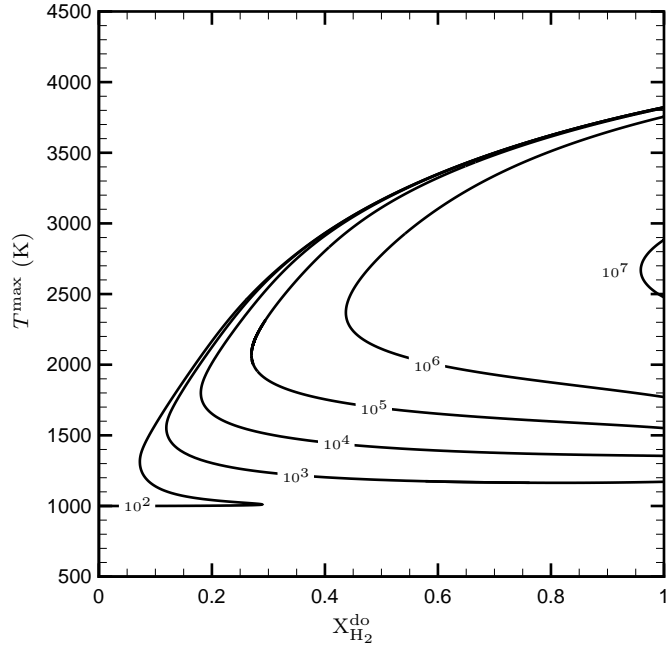


Figure 14: Maximal temperature of  $(\text{H}_2+\text{H}_2\text{O})\text{-O}_2$  flames

### 7.3 Flammability of $\text{H}_2\text{-O}_2$ mixtures

In order to study the flammability limits of  $\text{H}_2\text{-O}_2$  mixtures in a turbulent context, we consider the case of a symmetric premixed stretched flame at pressure  $p = 100$  atm. Both impinging jets are supposed to be at same temperature and composition and the strain rate  $\varepsilon$  is fixed at the value  $\varepsilon = 10000 \text{ s}^{-1}$ . By varying alternatively the temperature and the composition of the impinging jets with the aid of continuation techniques, it is possible to determine the lean and rich extinction limits of  $\text{H}_2\text{-O}_2$  premixed stretched flames for different injection temperature  $T^{\text{fr}}$ . Figure 18 represents the  $\varepsilon = 10000 \text{ s}^{-1}$  flammability domain in  $(\phi, T^{\text{fr}})$  coordinates,  $\phi$  being the equivalence ratio of the fresh mixture. This flammability domain is classically bounded by a lean extinction limit and a rich extinction limit. In real gas context, a thermodynamics related limit should also be taken into account. This limit is the stability limit of the fresh mixture under which no homogeneous mixture may exist thanks to thermodynamically driven demixing phenomena as evoked in Section 4. The rich extinction limit, represented by the solid line, meets the stability limit, represented by the dash-dotted line, at  $\phi = 4$  and  $T^{\text{fr}} = 68 \text{ K}$ . The lean extinction limit, represented by the dashed line, meets the stability limit at  $\phi = 0.11$  and  $T^{\text{fr}} = 73 \text{ K}$ . This feature induces that for reactant temperature below  $T^{\text{fr}} = 68 \text{ K}$  the two fluid phases appearing in the extinguished mixing layer are located outside the flammability domain which hinders reignition and may lead to engine-scale combustion instabilities.

## 8 Conclusion

In this study a general high pressure flame model has been implemented in a stretched flame solver. This model combines a thermodynamical description of dense fluid based on a Soave-Redlich-Kwong equation, nonideal high pressure transport coherent with thermodynamics of irreversible process, statistical mechanics and statistical non-equilibrium thermodynamics and a chemical representation using nonideal production rates.

The pseudo vaporization phenomenon which arise at the encounter of a dense transcritical oxygen jet with a hot oxygen jet has been adressed in Section 3. The position of the dense to dilute transition with respect to the stagnation point of the stretched structure is weakly sensitive to the shear viscosity model and so is the per unit surface pseudo-vaporization flux.

The structure of a cold  $\text{H}_2\text{-O}_2$  mixing layer has been studied in Section 4 and the nonideal transport modelling yields retrodiffusion effects which prevent the mixing of the two ergols when the temperature and pressure conditions approaches the thermodynamical stability limit for the mixture. This lack of

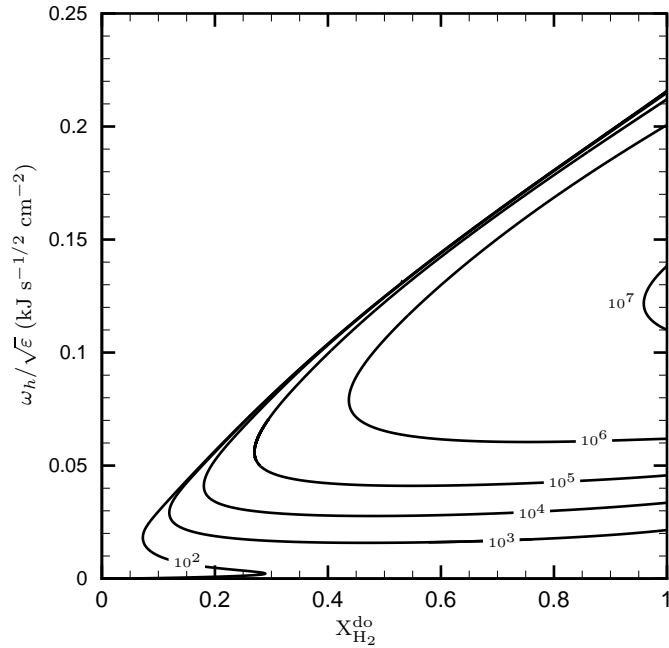


Figure 15: Reduced heat release per unit flame surface of  $(\text{H}_2+\text{H}_2\text{O})-\text{O}_2$  flames

miscibility leads to the appearance of two phase flow in the wake of a rocket injector in the case of local extinction phenomenon seems to be of great importance for the overall combustion stability by hindering reignition of cold mixing structure.

Various stretched flame structures involving transcritical oxygen have then been studied in Section 5 and 6. The influence of nonideality are limited to the oxygen density prediction since the heating due to the flame reduce quickly the impact of nonidealities outside the  $\text{O}_2$  dense core. The flame structure adapts itself to the nonideal retrodiffusing flux and the influence in term of global quantity such as the heat release per unit of flame is insignificant.

Extinction limits with respect to stretch rate and to mixture ratio of the flame existing between combustion products and transcritical oxygen have been determined numerically in Section 7. If unphysical flames, that is to say flames containing thermodynamically unstable state, have been encountered during these continuation procedures, these flames belongs to unstable or extinguished branch and does not alter the computed extinction limits. Flammability domain in a turbulent context of  $\text{H}_2-\text{O}_2$  mixtures has been also determined. In this case and for very low reactant temperatures, it has been shown that demixing phenomena may prevent mixture reignition. This underlines the strong connections between extinction limits of cold mixtures and thermodynamical nonidealities.

## References

- [1] A. Liñán, *The asymptotic structure of counterflow diffusion flames for large activation energies*, Acta Astronautica 1 (1974) 1007-1039.
- [2] P. A. Libby and F. A. Williams, *Structure of Laminar Flamelets in Premixed Turbulent Flames*, Combustion and Flame 44 (1982) 287-303.
- [3] P. A. Libby, A. Liñán and F. A. William, *Strained Premixed Laminar Flames with Nonunity Lewis Numbers*, Combust. Sci. Tech 34 (1983) 257-293.
- [4] P. A. Libby and F. A. William, *Strained Premixed Laminar Flames with Two Reaction Zones*, Combust. Sci. Tech 37 (1984) 221-252.
- [5] F. E. Marble and J. E. Broadwell, *The Coherent Flame Model for Turbulent Chemical Reactions*, PROJECT SQUID, Tech. Report TRW-9-PU, Purdue university.

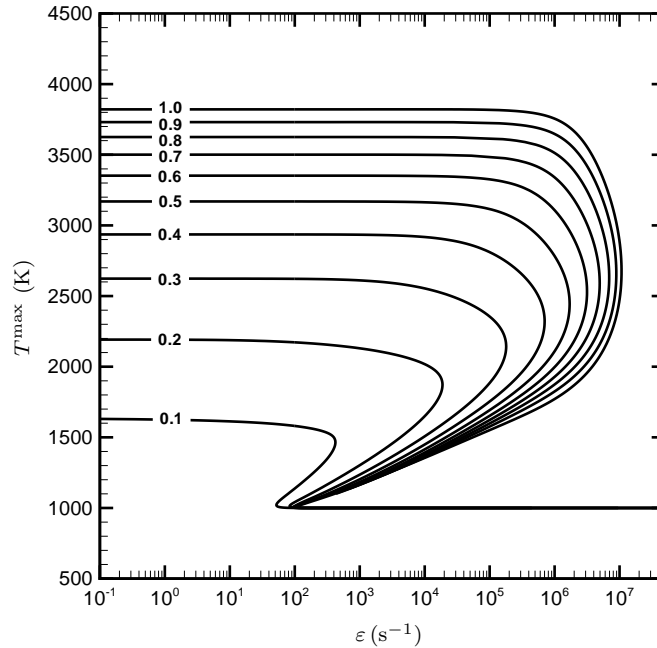


Figure 16: Maximal temperature of (H<sub>2</sub>+H<sub>2</sub>O)-O<sub>2</sub> flames

- [6] N. Peters, *Laminar diffusion flamelet models in non-premixed turbulent combustion*, Progress in Energy and Combustion Science 10 (1984) 319-339.
- [7] T. Poinso and D. Veynante, *Theoretical and Numerical Combustion*, R.T Edwards Ed., ISBN: 1-930217-05-6
- [8] A. M. Saur, F. Behrendt and E. U. Franck, *Calculation of High Pressure Counterflow Diffusion Flames up to 3000 bar*, Ber. Bunsenges. Phys. Chem 97 (1993) 900-908.
- [9] M. El-Gamal, E. Gutheil and J. Warnatz, *The Structure of Laminar Premixed H<sub>2</sub>-Air Flames at Elevated Pressures*, Zeit. Phys. Chem. 214 (2000) 419-435.
- [10] G. Ribert, N. Zong, V. Yang, L. Pons, N. Darabiha and S. Candel, *Counterflow diffusion flames of general fluids: Oxygen/hydrogen mixtures*, Combustion and Flame 154 (2009) 319-330.
- [11] L. Pons, N. Darabiha, S. Candel, G. Ribert and V. Yang, *Mass transfer and combustion in transcritical non-premixed counterflows*, Combustion Theory and Modelling 13 (2009) 57-81.
- [12] L. Pons, N. Darabiha, S. Candel, T. Schmitt and B. Cuenot, *The structure of multidimensional strained flames under transcritical combustion*, C. R. Mecanique 337 (2009) 517-527.
- [13] G. S. Soave, *Equilibrium constants from a modified Redlich-Kwong equation of state*, Chem. Eng. Sci 27 (1972) 157-172.
- [14] V. Giovangigli, L. Matuszewski and F. Dupoirieux, *Detailed modeling of planar transcritical H<sub>2</sub>-O<sub>2</sub>-N<sub>2</sub> flames*, Combust. Theory Mod. 15 (2011) 141-182.
- [15] N. Zong and V. Yang, *Cryogenic fluid jets and mixing layers in transcritical and supercritical environments*, Combust. Sci. Tech. 178 (2006) 193-227.
- [16] N. Zong and V. Yang, *Near-flow and flame dynamics of LOX/methane shear-coaxial injector under supercritical conditions*, Proc. Combust. Inst 30 (2007) 2309-2317.
- [17] J. Meixner, *Zur Thermodynamik der Thermodiffusion*, Ann. der Phys. 39 (1941) 333-356.
- [18] J. Meixner, *Zur Thermodynamik der irreversiblen Prozesse in Gasen mit chemisch reagierenden, dissoziierenden und anregbaren Komponenten*, Ann. der Phys 43 (1943) 244-270.

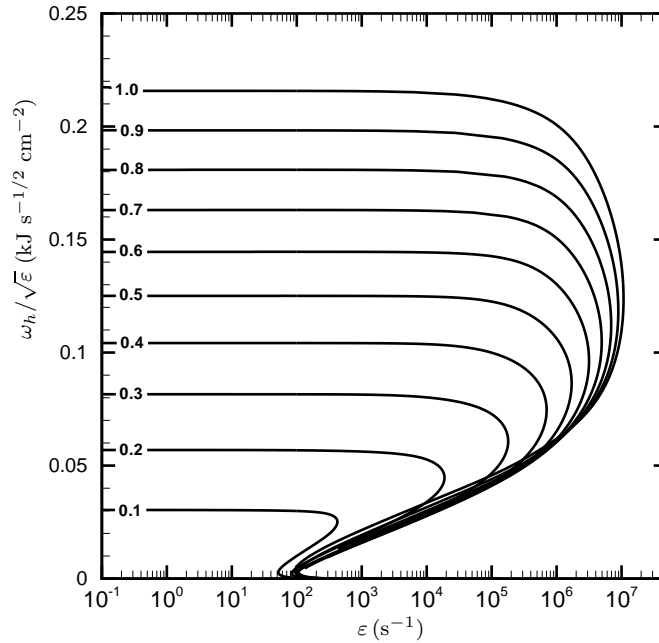


Figure 17: Reduced heat release per unit flame surface of (H<sub>2</sub>+H<sub>2</sub>O)-O<sub>2</sub> flames

- [19] I. Prigogine, *Étude Thermodynamique des Phénomènes Irréversibles*, Dunod, Paris (1947).
- [20] S. R. de Groot and P. Mazur, *Non-equilibrium Thermodynamics*, Dover, New York, (1984).
- [21] J. H. Irving and J. G. Kirkwood, *The statistical mechanics of transport processes. IV. The equations of hydrodynamics*, J. Chem. Phys. 18 (1950) 817-829.
- [22] R. J. Bearman and J. G. Kirkwood, *The statistical mechanics of transport processes. XI. Equations of transport in multicomponent systems*, J. Chem. Phys. 28 (1958) 136-145.
- [23] H. Mori, *Statistical-mechanical theory of transport in fluids*, Phys. Rev. 112 (1958) 1829-1842.
- [24] J. Keizer, *Statistical Thermodynamics of Nonequilibrium Processes*, Springer Verlag, New York (1987)
- [25] H. Van Beijeren and M. H. Ernst, *The modified Enskog equations*, Phys. A 68 (1973) 437-456.
- [26] H. Van Beijeren and M. H. Ernst, *The modified Enskog equations for mixture*, Phys A 70 (1973) 225-242.
- [27] V. I. Kurochkin, S. F. Makarenko and G. A. Tirskaa, *Transport coefficients and the Onsager relations in the kinetic theory of dense gas mixtures*, J. Appl. Mech. Tech. Phys. 25 (1984) 218-225
- [28] N. A. Okong'o and J. Bellan, *Direct numerical simulation of a transitional supercritical binary mixing layer: heptane and nitrogen*, J. Fluid Mech. 464 (2002) 1-34.
- [29] J. C. Oefelein, *Thermophysical characteristics of shear-coaxial LOX-H<sub>2</sub> flames at supercritical pressure*, Proc. Combust. Inst. 30 (2005) 2929-2937.
- [30] J. Bellan, *Theory, modeling and analysis of turbulent supercritical mixing*, Combust. Sci. Tech 178 (2006) 253-281.
- [31] M. R. Marcelin, *Sur la mécanique des phénomènes irréversibles*, Comptes rendus hebdomadaires des séances de l'Académie des Sciences, Ed. Gauthier-Villars (1910) 1052-1055.
- [32] M. R. Marcelin, *Contribution à l'étude de la cinétique physico-chimique*, PhD thesis, Faculté des Sciences de Paris (1914)
- [33] A. Ern and V. Giovangigli, *The kinetic equilibrium regime*, Phys. A 260 (1998) 49-72.

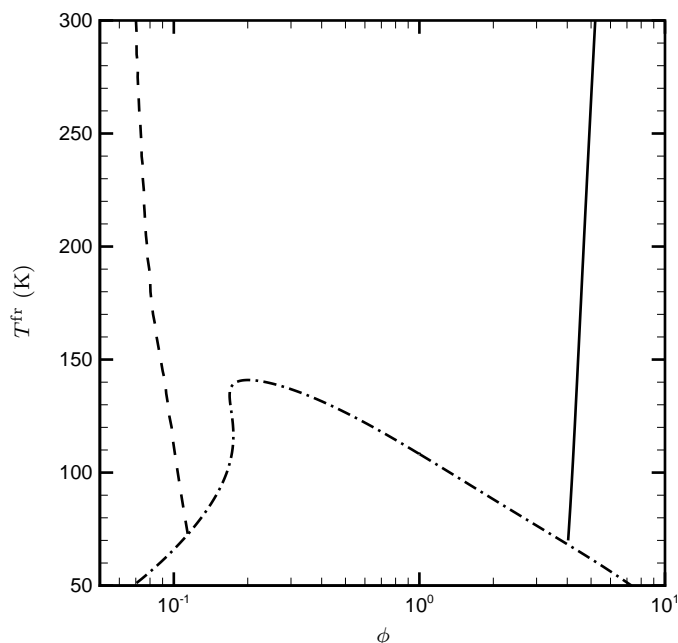


Figure 18: Flammability domain of H<sub>2</sub>-O<sub>2</sub> mixtures under a  $\varepsilon = 10000 \text{ s}^{-1}$  stretch rate at pressure  $p = 100 \text{ atm}$ . —: Rich extinction limit, - - -:Lean extinction limit, - · -:Stability limit.

- [34] V. Giovangigli, *Multicomponent Flow Modeling*, Birkhäuser, Boston (1999).
- [35] V. Yang, *Modeling of supercritical vaporization, mixing and combustion processes in liquid-fueled propulsion systems*, Proc. Combust. Inst. 28 (2000) 925-942.
- [36] L. J. Gillespie, *Equilibrium pressures of individual gases in mixtures and the mass-action law for gases*, J. Am. Chem. Soc. 47 (1925) 305-312.
- [37] J. A. Beattie, *The computation of the thermodynamic properties of real gases and mixtures of real gases*, Chem. Rev. 18 (1948) 141-192.
- [38] R. C. Reid, J. M. Prausnitz and B. E. Poling, *The Properties of gases and Liquids*, McGraw-Hill, New York (1987).
- [39] V. Giovangigli and L. Matuszewski, *Supercritical fluid thermodynamics from equation of state*, (in preparation)
- [40] M. Benedict, G. B. Webb and L. C. Rubin, *An empirical equation for thermodynamics properties of light hydrocarbons and their mixture. I. Methane, Ethane, Propane and n-Butane.*, J. Chem. Phys. 8 (1940) 241-256.
- [41] G. S. Soave, *An effective modification of the Benedict-Webb-Rubin equation of state*, Fluid Phase Equil. 164 (1999) 157-172.
- [42] O. Redlich and J.N.S. Kwong, *On the thermodynamics of solution, V. An equation of state. Fugacities of gaseous solutions*, Chem. Rev. 44 (1949) 223-244.
- [43] D. Y. Peng and D. B. Robinson, *A new two-constant equation of state*, Indust. Eng. Chem. Fund. 15 (1976) 59-64.
- [44] K.G. Harstad, R.S. Miller and J. Bellan, *Efficient high pressure state equations*, AIChE J. 43-6 (1997) 1605-1610.
- [45] L. Verlet, *Computer "experiments" on classical fluids. I. Thermodynamical properties of Lennard-Jones molecules*, Phys. Rev. 159 (1967) 98-103.

- [46] W. A. Cañas-Marín, U. E. Guerrero-Aconcha and J. D. Ortiz-Arango, *Comparison of different cubic equations of state and combination rules for predicting residual chemical potential of binary and ternary Lennard-Jones mixtures: Solid-supercritical fluid phase equilibria*, Fluid Phase Equil. 234 (2005) 42-50.
- [47] W. A. Cañas-Marín, J. D. Ortiz-Arango, U. E. Guerrero-Aconcha and C. P. Soto-Tavera, *Thermodynamic derivative properties and densities for hyperbaric gas condensates: SRK equation of state prediction versus Monte-Carlo data*, Fluid Phase Equil. 253 (2007) 147-154.
- [48] J. O. Hirschfelder, C. F. Curtiss and R. B. Bird, *Molecular Theory of Liquid and Gases*, (2nd ed.) Wiley and Sons, New York (1964).
- [49] G. M. Wilson, *Vapor-liquid equilibria correlated by means of a modified Redlich-Kwong equation of state*, Adv. Cryog. Eng. 9 (1964) 168-176.
- [50] M. S. Grabovski and T. E. Daubert, *A modified Soave equation of state for phase equilibrium calculations. 3. Systems containing hydrogen*, Ind. Eng. Chem. Process. Dev. Des. 18 (1979) 300-306.
- [51] E. D. Ozokwelu and J. H. Erbar, *An improved Soave-Redlich-Kwong equation of state*, Chem. Rev. A 45 (1987) 9-19.
- [52] L. Waldmann, *Transporterscheinungen in Gasen von mittlerem Druck*, Handbuch der Physik 12 (1958) 258-514.
- [53] J. Van de Ree, *On the definition of the diffusion coefficients in reacting gases*, Physica 36 (1967) 118-126.
- [54] S. Chapman and T. G. Cowling, *The Mathematical Theory of Non-Uniform Gases*, Cambridge University Press, Cambridge (1970).
- [55] J. H. Ferziger and H. G. Kaper, *Mathematical Theory of Transport Processes in Gases*, North-Holland, Amsterdam (1972).
- [56] M. Ó Conaire, H. J. Curran, J. M. Simmie, W. J. Pitz and C. K. Westbrook, *A Comprehensive Modeling Study of Hydrogen Oxidation*, Int. J. Chem. Kin. 36 (2004) 603-622.
- [57] M. A. Mueller, T. J. Kim, R. A. Yetter and F. L. Dryer, *Flow Reactor Studies and Kinetic Modeling of the H<sub>2</sub>/O<sub>2</sub> Reaction*, Int. J. Chem. Kin. 31 (1999) 113-125.
- [58] M. D. Smooke, *Solution of burner stabilized premixed laminar flames by boundary value methods*, J. Comp. Phys., 48 (1982) 72-105
- [59] V. Giovangigli and M. D. Smooke, *Adaptive continuation algorithm with application to combustion problems*, Appl. Num. Math. 5 (1989) 305-331.
- [60] V. Giovangigli and N. Darabiha, *Vector Computers and Complex Chemistry Combustion*, Mathematical Modeling in Combustion and Related Topics (Brauner C and Schmidt-Laine C Eds. Ni-jhoffM Pug.) NATO ASI Series, 140 (1988) 491-503.
- [61] A. Ern and V. Giovangigli, *Multicomponent Transport Algorithms*, Lecture Notes in Physics, New Series "Monographs", m 24, (1994)
- [62] A. Ern and V. Giovangigli, *Thermal Conduction and Thermal Diffusion in Dilute Polyatomic Gas Mixtures*, Physica A 214 (1995) 526-546.
- [63] A. Ern and V. Giovangigli, *Optimized Transport Algorithm for Flame Codes*, Comb. Sci. Tech. 118 (1996) 387-395.
- [64] A. Ern and V. Giovangigli, *EGlib server and user's manual*, <http://www.cmap.polytechnique.fr/www.eglib/>
- [65] A. Ern and V. Giovangigli, *Projected Iterative Algorithms with Application to Multicomponent Transport*, Linear Algebra and its Applications 250 (1997) 289-315.
- [66] S. Jay, F. Lacas and S. Candel, *Combined surface density concepts for dense spray combustion*, Comb. and Flame 144 (2006) 558-577.